

# Design of Hybrid-Storage-Based Virtual Synchronous Machine With Energy Recovery Control Considering Energy Consumed in Inertial and Damping Support

Chu Sun<sup>✉</sup>, Member, IEEE, Syed Qaseem Ali<sup>✉</sup>, Member, IEEE, Geza Joos<sup>✉</sup>, Life Fellow, IEEE, and François Bouffard<sup>✉</sup>, Senior Member, IEEE

**Abstract**—The reduced inertia in power system introduces more operation risks and challenges due to the degraded frequency performance. The existing virtual inertia control and fast frequency response to tackle this issue are restricted by the energy resource behind the power converter. In this article, an improved virtual synchronous machine control is proposed, considering the limitation of energy storage in response speed and energy capacity. The fast-acting energy storage system is used to emulate inertia and damping. The energy consumed by both services in dynamic process and steady-state state is also investigated. An energy recovery control is designed to restore the energy consumed in inertia emulation and damping provision, thereby ensuring constant energy reserve. Besides, the slow-acting energy storage with larger energy capacity, is controlled like the governor regulator of synchronous generator and capable of providing long-term energy service. A design procedure considering storage limitation, control stability, and bandwidth separation is proposed. Effectiveness of the proposed control and design is validated by comprehensive simulation and hardware test results.

**Index Terms**—Bandwidth separation, energy consumption, energy recovery, hybrid energy storage, virtual synchronous machine.

## I. INTRODUCTION

WITH the rapid proliferation of renewable energy resources such as wind and photovoltaic (PV), the inertia in power system is undergoing a gradual decrease, which may result in higher rate of change of frequency (RoCoF) and larger

Manuscript received December 19, 2020; revised April 23, 2021; accepted August 24, 2021. Date of publication September 10, 2021; date of current version November 30, 2021. Recommended for publication by Associate Editor P. Mattavelli. (*Corresponding author: Chu Sun*.)

Chu Sun was with the Department of Electrical Engineering, McGill University, Montreal, QC H3A 0G4, Canada. He is now with the School of Automation Science and Electrical Engineering, Beihang University, Beijing 100191, China (e-mail: sunchu@buaa.edu.cn; chu.sun@mail.mcgill.ca).

Syed Qaseem Ali is with Application eXpertise and Electrical Simulation, OPAL-RT Technologies Inc., Montreal, QC H3K 1G6, Canada (e-mail: sqali@ieee.org).

Geza Joos and François Bouffard are with the Department of Electrical and Computer Engineering, McGill University, Montreal, QC H3A 0G4, Canada (e-mail: geza.joos@mcgill.ca; francois.bouffard@mcgill.ca).

Color versions of one or more figures in this article are available at <https://doi.org/10.1109/TPEL.2021.3111482>.

Digital Object Identifier 10.1109/TPEL.2021.3111482

frequency deviation after a contingency event [1]. This also leads to more sophisticated regulation efforts and, thus, wear-and-tear of conventional generation units [2], or even triggers faulty protection action. To improve frequency performance, various grid support strategies are proposed for inverter-based resources based on the existing grid-following control, which can be generally classified into three types [3]: event/step-based synthetic inertia (SI), derivative SI, proportional frequency response (droop). All these strategies can be categorized into fast frequency response (FFR) as a general intermediate action between synchronous inertial response and primary frequency control [4]. A review of the FFR services are found in [5], which compares the droop slope, response time, and procurement of different FFR. In [6], FFR and SI are distinguished as the power response in proportion to the deviation of frequency and the RoCoF, respectively. Multiple endeavors are made to provide improved FFR services by wind turbine generator, HVdc system [7], [8], dynamic load [9] with the aid of wide area monitoring system or online parameter estimation [10] under the constraints of wind generator rotor speed [11], the limited capacity of energy storage system (ESS) [12] and PV plants [13]. However, the control performance of FFR is limited in response speed and cannot work independently partially due to the stability and synchronization issue of phase-locked loop used in grid-following control [14].

In recent years, virtual synchronous machine (VSM), with self-synchronization and black-start capability, receives widespread attention [15], [16]. The National Grid ESO in U.K. has launched a research program called VSM Expert Group to promote VSM application [17]. The State Grid in China has launched several trial standards on VSM design [18]. The widely discussed topics in recent years include the applicability for different impedance [19], stability and damping [20]–[25], power decoupling [26], [27], and fault tolerant control [28]. An ideal dispatchable dc source is usually assumed in most studies, which does hold for most devices in the present power system. With rechargeable and partially controllable capability, ESS is more promising for practical VSM implementation than renewable resource. However, the inherent technical downsides

restrict the application of ESS operating as VSM to provide inertia and damping service.

First, ESS is limited in the power and energy capacity by which they can be broadly categorized into two types: short-term power type such as supercapacitor, lithium-ion capacitor and flywheel, and long-term energy type including pumped hydro, compressed air and chemical battery [29]. To accumulate the energy required for virtual inertia, some researchers proposed VSM implementation based on dc microgrid [30] or dc microgrid [31], and additional droop control is utilized to distribute power between energy storage units. However, most of the theoretical analysis is on control stability, but the sizing of the energy storage is ignored. To determine the capacity of storage of VSM, Soni *et al.* [32] investigated the energy variation for droop-based control and VSM. The dc capacitor is exploited to supply the energy for VSM under the constraints of dc voltage and control stability under multiple scenarios [33], [34]. However, these studies mainly consider the frequency nadir and the energy amount in the inertial support. In contrast, there are numerous studies of VSM participating in oscillation damping [35], for which the energy consumption and storage sizing are rarely discussed. Yuan *et al.* [36] analyzed the energy variation and sizing of VSM in critical damping, overdamping and underdamping cases, but the analysis is restricted to single machine infinite bus system rather than a general network with other generators.

Second, the services provided by VSM is subject to the response speed of ESS, by which they can be divided into fast-acting ESS (FAESS) and slow-acting ESS (SAESS). Short-term ESS with large power density and high response speed (depending on its C rate) usually belongs to FAESS. By contrast, long-term ESS with higher energy density but lower response speed, usually falls into SAESS category. A single energy storage unit with both high power and energy capacity, such as Lead–Carbon ultrabattery and lithium titanate battery, is still immature for large-scale deployment [37]. By proper hybridization of both types of ESS, their advantages can be supplemented while drawbacks avoided. The architecture of hybridization can be generally classified into three types: cascade, passive parallel and active parallel [38], [39]. In [40], an advanced VSM based on hybrid energy storage is introduced, where the supercapacitor tracks the fast-varying power component while the battery storage compensates for the slow-varying component. Similar research work is found in [41], with an energy management system added to distribute power in different scenarios. However, the impact of the storage characteristics on VSM parameter design are not explicitly presented.

Third, the state-of-charge (SoC) of battery storage should be retained within an acceptable range to avoid unexpected damages. To address this limitation, a SoC feedback control for VSM based on hybrid storage is proposed in [42] to avoid over-charging/discharging of storage, but such feedback is SoC limit triggered, which cannot ensure constant reserve for continuous operation. Shim *et al.* [43] put forth an improved VSM implementation based on type-IV wind turbine generator and short-term ESS whose SoC is managed by additional proportional–integral (PI) control, and the energy for inertia

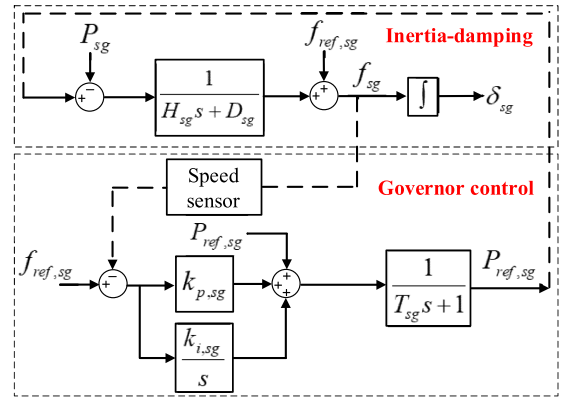


Fig. 1. Diagram of frequency control for synchronous generator.

emulation is also quantified. However, the design of PI parameters are not presented. A harmonious integration of synchronous generator and FAESS with virtual inertia control is described in [44], where an SoC feedback control is added to secure SoC at the desired level. However, such control design based on grid-following droop cannot be directly applied to grid-forming VSM. Moreover, none of the above studies explored the impact of SoC recovery design on frequency control and the bandwidth separation requirement.

Based on the literature review and first principle thinking, it can be concluded that the practically available resource such as ESS has become the bottleneck of implementing VSM to provide any inertia or oscillation damping services. For this, a guideline, mainly from the energy perspective, for control and design of VSM based on hybrid energy storage in both dc and ac coupled schemes is introduced in this article, following our precedent work in [45]. The contributions of the article mainly include the following aspects and are validated with comprehensive simulation and hardware tests.

- 1) Not only the energy consumed by FAESS in inertia but also in damping support is analytically quantified. It is the first time revealed that the steady-state energy variation is proportional to the damping value while reciprocal to the integral gain of secondary frequency control in the system.
- 2) A complete procedure is proposed to size the storage and design the virtual inertia, damping and governor parameters of VSM, considering multiple factors including the maximum energy consumption, control stability requirement, bandwidth separation, as well as the practical storage characteristics.
- 3) The proportional and integral gains of energy recovery control are designed based on bandwidth separation and stability requirement, by which the SoC of FAESS is around a desired value without adversely affecting frequency control.

## II. VSM CONTROL STRATEGY BASED ON HYBRID ENERGY STORAGE

As illustrated in Fig. 1, the inertia and damping part of synchronous generator (SG) and its governor control can be

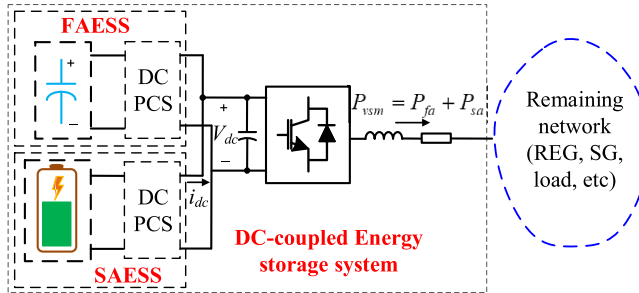


Fig. 2. Diagram of dc-decoupled FAESS and SAESS.

emulated by FAESS and SAESS, respectively, given their characteristics of response speed and energy capacity [40].

#### A. DC-Coupled Scheme

FAESS and SAESS are connected in parallel to a common inverter with two bidirectional dc power conversion system (PCS), as shown in Fig. 2 [40], [45]. The control strategy for the common inverter is a combination of inertia and damping emulation as well as virtual governor control. The stored energy in FAESS can be evaluated by a SoC-alike index. For rotational SG, the energy variation in inertial response will be automatically restored as the rotor speed returns to normal, but this does hold for FAESS given the decoupling of frequency and energy. For this, an energy recovery control is added to the power reference of FAESS, with typical SoC reference at 0.5. A leading term  $T_{hs}$  may also be added to suppress the oscillation associated with VSM [21]. Reactive power is controlled at constant by PI control, without incurring power coupling and reactive power circulation.

It is illustrated in Fig. 3 that the dc PCS interfacing FAESS is controlled to maintain constant dc voltage on the common bus, while the dc PCS of SAESS will follow the power reference from virtual governor control. In this way, FAESS will automatically supply the fast-varying components, while SAESS will track the slow-varying components. An integral control may be also added to recover frequency if the SAESS acts as the slack bus.

#### B. AC-Coupled Scheme

This article mainly focuses on ac-coupled scheme, which integrates the inertia and governor parts with two separate inverters, as shown in Fig. 4. The energy recovery control of FAESS is shown in Fig. 5(a). The SAESS adopts PLL for grid-synchronization and droop control to emulate the governor response, as shown in Fig. 5(b). The ac-coupled and dc-coupled scheme can be treated approximately equivalent, except the PLL dynamics of SAESS.

#### C. Comparison Between DC- and AC-Coupled Scheme

The dc and ac coupled schemes are similar to the semiactive and active parallel of hybrid storage in [38]. Both schemes are compared in [39], with more insights given as follows.

- 1) The dc-coupled scheme has more compact installation. However, the power required by both inertia-damping emulation and longer-time regulation will flow through the single inverter, thus, not saving the total power capacity of power converters. Besides, at least one dc-PCS is needed for the dc-coupled case to separate the power of both storage, which can be exempted in the ac case. Therefore, which scheme has lower cost in power switches is controversial.
- 2) The ac-coupled scheme can be installed more flexibly in the ac dominant power system. The FAESS and SAESS can be installed separately in different locations, such as FACTS devices, EV charging stations, controllable loads, HVdc systems, microgrids, or wind/PV farms.
- 3) The ac coupled scheme is superior in terms of reliability and protection. Due to the tightly coupled feature, failure of the common inverter, or any dc PCS in the dc-coupled scheme, will lead to the dysfunction of the entire VSM. By contrast, either virtual governor control or inertia-damping control can still work in such conditions. In case of fault, the fuse clearance in ac circuit will also be easier than in the dc counterpart.

#### D. Power System Studied

A general power network used to verify the control strategy is shown in Fig. 6, consisting of an SG, a renewable energy generator, an active power load, and one or multiple energy storage systems. The total inertia of the original system is low, with high penetration of power-electronic converters. The renewable energy generator adopting maximum power-point tracking control is regarded as negative loads in the power-balance study.

### III. DYNAMIC ANALYSIS AND FAESS SIZING

#### A. Modeling of Active Power and Frequency Dynamics

With frequency and active power control as the research focus, simplified models are established by ignoring the disturbance of reactive power/voltage control and the fast dynamics in the inner current and voltage control loops.

1) *SAESS Modeling*: Compared with dc-coupled case, the SAESS in ac-coupled case should be given more attention due to the impact of PLL [46]. In the detailed model of Fig. 7, the  $q$ -axis voltage ( $v_{o,q}$ ) affecting the grid phase angle will be a disturbance to current control through the path of  $G_{PLL}(s)$  [denoted as (1)]. To ensure fast and precise current control, the bandwidth (approximated by  $\sqrt{k_{i,PLL}}$ , usually at tens Hz) of a well-designed PLL is much smaller than current control [ $H_{ci}(s)$ ]. Therefore, system frequency and PLL usually have little impact on the  $d$ -axis current and, thus, active power control

$$\theta = \frac{T_{PLL}(s)}{s + V_d T_{PLL}(s)} v_{o,q} = G_{PLL}(s) v_{o,q}$$

$$T_{PLL}(s) = k_{p,PLL} + k_{i,PLL} \frac{1}{s}. \quad (1)$$

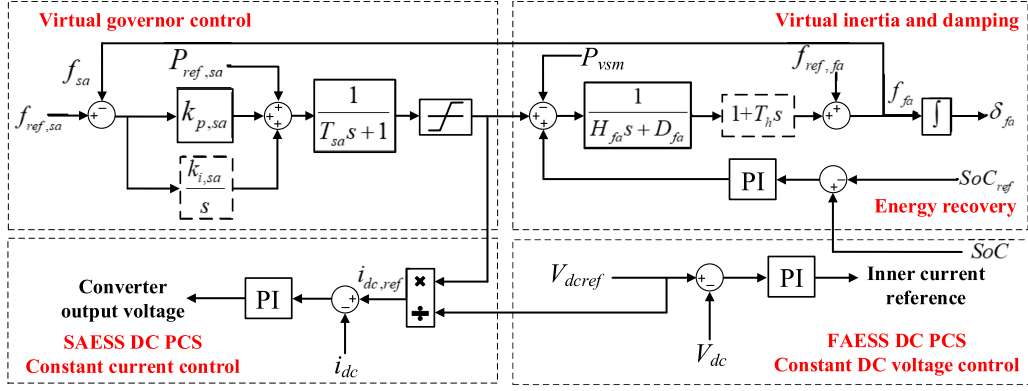


Fig. 3. Power and frequency control block for VSM based on dc-coupled FAESS and SAESS.

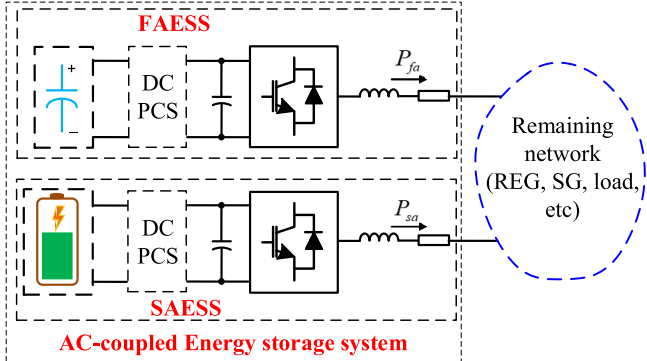


Fig. 4. Diagram of ac-decoupled FAESS and SAESS.

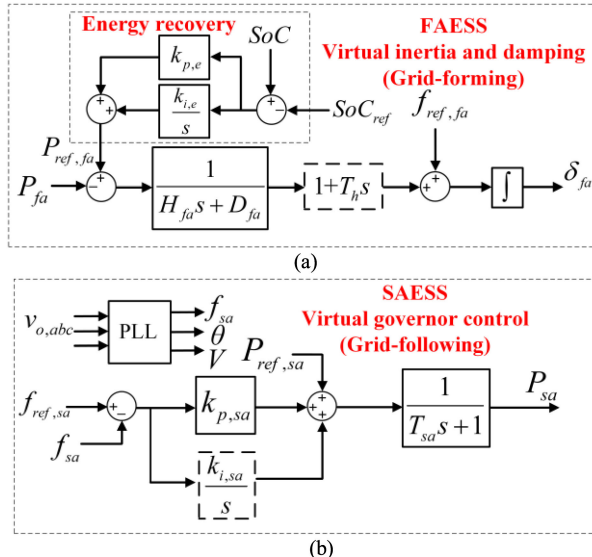


Fig. 5. Diagram of VSM control based on ac-coupled hybrid storage. (a) Control of FAESS. (b) Control of SAESS.

Although PLL indeed introduces a small delay in frequency measurement, its effect can be ignored compared with the time-constant of virtual governor control. Therefore, for both ac and

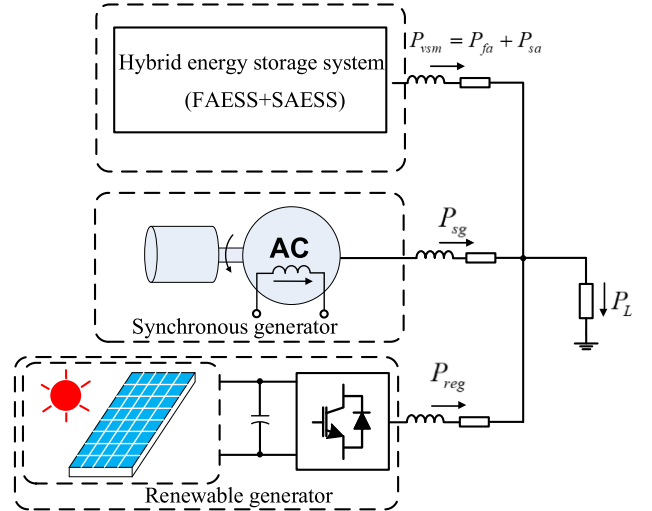


Fig. 6. Configuration of the studied power system.

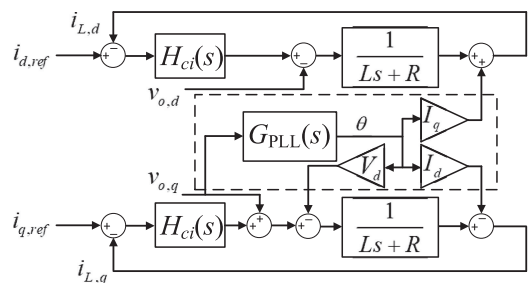


Fig. 7. Model of DQ current control within SAESS considering the PLL effect.

dc-coupled case, the power of SAESS ( $\Delta P_{sa}$ ) is given by

$$\Delta P_{sa} = -\frac{k_{p,sa}}{T_{sa}s + 1}\Delta f_{sa} \approx -\frac{k_{p,sa}}{T_{sa}s + 1}\Delta f_{fa} \quad (2)$$

where  $k_{p,sa}$  is the droop gain, and  $T_{sa}$  represents the response time in virtual governor control. As SAESS is installed near FAESS, their frequency ( $f_{sa}$  and  $f_{fa}$ ) can be treated equal.

2) *Modeling of FAESS, Emulated SG, and the Overall System:* An approximate model for both schemes considering the

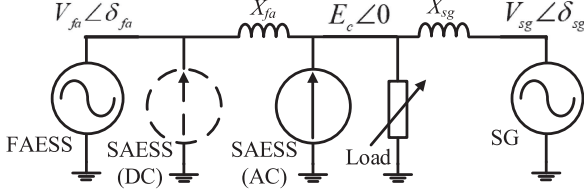


Fig. 8. Single-line diagram of the system.

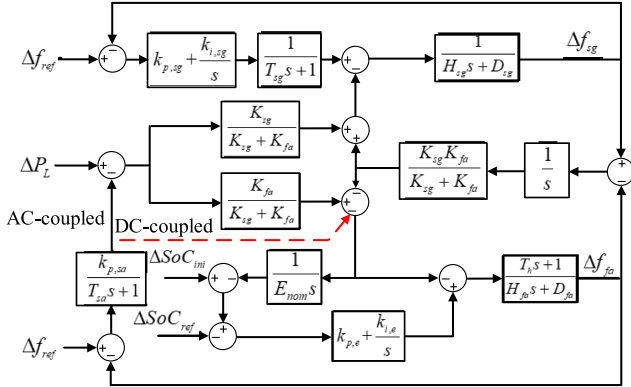


Fig. 9. Detailed model of active power and frequency dynamics in the system.

impedance dynamics of the system is presented here. Based on Fig. 8, the transient sharing of power mismatch ( $\Delta P_{\text{mis}}$ ) between synchronous generator ( $\Delta P_{\text{sg}}$ ) and FAESS ( $\Delta P_{\text{fa}}$ ) is given by (3), where  $\delta$ ,  $V$ , and  $X$  denote the phase angle, voltage magnitude, and connecting reactance, respectively, while the subscripts “sg” and “fa” correspond to SG and FAESS

$$\begin{aligned} \Delta P_{\text{mis}} &= \Delta P_L - \Delta P_{\text{sa}} \\ \Delta P_{\text{sg}} &= \frac{K_{\text{sg}}}{K_{\text{sg}} + K_{\text{fa}}} \Delta P_{\text{mis}} + \frac{K_{\text{sg}} K_{\text{fa}}}{K_{\text{sg}} + K_{\text{fa}}} (\Delta \delta_{\text{sg}} - \Delta \delta_{\text{fa}}) \\ \Delta P_{\text{fa}} &= \frac{K_{\text{fa}}}{K_{\text{sg}} + K_{\text{fa}}} \Delta P_{\text{mis}} + \frac{K_{\text{sg}} K_{\text{fa}}}{K_{\text{sg}} + K_{\text{fa}}} (\Delta \delta_{\text{fa}} - \Delta \delta_{\text{sg}}) \\ K_{\text{sg}} &= V_{\text{sg}} E_c \cos \delta_{\text{sg}} / X_{\text{sg}}, \quad K_{\text{fa}} = V_{\text{fa}} E_c \cos \delta_{\text{fa}} / X_{\text{fa}}. \end{aligned} \quad (3)$$

For the virtual inertia-damping control, the power–frequency relation of FAESS is given by (4), in which  $H_{\text{fa}}$ ,  $D_{\text{fa}}$ , and  $T_h$  are the inertia time constant, damping, and leading time constant of FAESS. The power associated with energy recovery control is ignored here since it is a slow process

$$-\frac{T_h s + 1}{H_{\text{fa}} s + D_{\text{fa}}} (\Delta P_{\text{ref,fa}} - \Delta P_{\text{fa}}) = -\Delta f_{\text{fa}}. \quad (4)$$

In addition, the energy recovery control yields the power reference of FAESS  $P_{\text{ref,fa}}$ , which is modeled as (5) where  $k_{p,e}$  and  $k_{i,e}$  are the proportional and integral gain of energy recovery control,  $SoC_{\text{ini}}$  and  $E_{\text{nom}}$  are, respectively, the initial SoC and the energy capacity of FAESS

$$\Delta P_{\text{ref,fa}} = -(k_{p,e} + k_{i,e}/s)(\Delta SoC_{\text{ref}} - \Delta SoC)$$

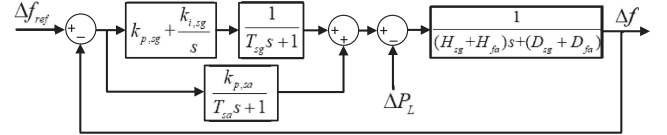


Fig. 10. Simplified diagram of system frequency control.

$$\Delta SoC = \Delta SoC_{\text{ini}} - \Delta P_{\text{fa}} / (E_{\text{nom}} s). \quad (5)$$

For SG, the inertia-damping and frequency control yield the relation (6) and (7), where  $H_{\text{sg}}$  and  $D_{\text{sg}}$  are the inertia time constant and damping value,  $k_{p,sg}$  and  $k_{i,sg}$  are the droop and integral gain for primary and secondary frequency control

$$-(\Delta P_{\text{ref,sg}} - \Delta P_{\text{sg}}) / (H_{\text{sg}} s + D_{\text{sg}}) = -\Delta f_{\text{sg}} \quad (6)$$

$$(k_{p,sg} + k_{i,sg}/s) \frac{-\Delta f_{\text{sg}}}{T_{\text{sg}} s + 1} = \Delta P_{\text{ref,sg}}. \quad (7)$$

Based on the above-mentioned analysis, the overall system is modeled and shown in Fig. 10. This model will be useful especially when the transient power sharing or inter-oscillation among (virtual) synchronous generators is concerned [21].

### B. Quasi-Steady-State Power Sharing

Focused on system averaged frequency, a uniform and approximate analysis for both ac and dc coupled cases is given here. The locational impact of inertia is ignored and frequency in the system is assumed identical everywhere, as denoted by (8). The leading term  $T_h s$  for mitigating the interoscillation between (virtual) synchronous generators is also omitted. Such assumption and simplification are reasonable especially for small networks with short feeders [47].

$$\Delta f_{\text{sa}} \approx \Delta f_{\text{sg}} \approx \Delta f_{\text{fa}} = \Delta f. \quad (8)$$

The disturbance from energy recovery control in the frequency control is initially ignored and will be considered in Section IV. The total power disturbance  $\Delta P_L$  is balanced by FAESS, SAESS, and SG, as formulated by

$$\Delta P_{\text{fa}} + \Delta P_{\text{sg}} + \Delta P_{\text{sa}} = \Delta P_L. \quad (9)$$

The overall frequency control can be simplified, as in Fig. 10. Therefore, the dynamics of system frequency and power of FAESS and SG are derived as

$$\begin{aligned} \Delta f(s) &= G_f(s) \Delta P_L \\ &= \frac{(T_{\text{sg}} s + 1)(T_{\text{sa}} s + 1)s}{((H_{\text{sg}} + H_{\text{fa}})s + D_{\text{sg}} + D_{\text{fa}})(T_{\text{sg}} s + 1)(T_{\text{sa}} s + 1)s + k_{p,sa}s(T_{\text{sg}} s + 1) + (k_{p,sg}s + k_{i,sg})(T_{\text{sa}} s + 1)} \Delta P_L \end{aligned} \quad (10)$$

$$\Delta P_{\text{fa}}(s) = -(H_{\text{fa}} s + D_{\text{fa}}) \Delta f(s) \quad (11)$$

$$\Delta P_{\text{sg}}(s) = -\left(\frac{k_{p,sg} + k_{i,sg}/s}{T_{\text{sg}} s + 1} + (H_{\text{sg}} s + D_{\text{sg}})\right) \Delta f(s). \quad (12)$$

For a given frequency disturbance ( $\Delta f$ ),  $\Delta P_{fa}(s)$  is a high-pass filter process, while  $\Delta P_{sa}(s)$  is a low-pass filter process. The initial RoCoF and the rate-of-change-of-power (RoCoP) of SAESS can be estimated by (13) and (14), using the final-value theorem. The increased inertia of FAESS will reduce system RoCoF and the RoCoP of SAESS, thus relaxing the response speed demand on SAESS and increasing frequency stability

$$\frac{d\Delta f}{dt}|_{t=0} = s^2 \Delta f(s)|_{s \rightarrow \infty} = \frac{\Delta P_L}{H_{sg} + H_{fa}} \quad (13)$$

$$\frac{d\Delta P_{sa}(t)}{dt}|_{t=0} = s^2 \Delta P_{sa}(s)|_{s \rightarrow \infty} = \frac{k_{p,sa}}{(H_{sg} + H_{fa})T_{sa}} \Delta P_L \quad (14)$$

$$\Delta P_{sg}|_{t=0} = s \Delta P_{sg}(s)|_{s \rightarrow \infty} = H_{sg} \Delta P_L / (H_{sg} + H_{fa}) \quad (15)$$

$$\Delta P_{fa}|_{t=0} = s \Delta P_{fa}(s)|_{s \rightarrow \infty} = H_{fa} \Delta P_L / (H_{sg} + H_{fa}). \quad (16)$$

FAESS and SG will share the transient power mismatch in proportion to their inertia values, as (15), (16) indicates. The steady-state power is estimated by  $\Delta P_{sa}(s)|_{s \rightarrow 0} = 0$ ,  $\Delta P_{fa}(s)|_{s \rightarrow 0} = 0$ ,  $\Delta P_{sg}(s)|_{s \rightarrow 0} = \Delta P_L$ , due to the secondary frequency control of SG.

### C. Sizing of FAESS

If the maximum energy variation of FAESS ( $\Delta E_{max}$ ) is known, its nominal energy capacity  $E_{nom}$  can be determined by

$$E_{nom} = \Delta E_{max} / (\Delta E_{max}/E_{nom}) = \frac{\Delta E_{max}}{\Delta E\%_{max,allowed}} \quad (17)$$

where  $\Delta E\%_{max,allowed}$  denotes the maximum energy percentage allowed in normal operation. The maximum energy variation of FAESS in inertial response, damping support, and the whole dynamic process is investigated first.

1) *Energy Variation Due to Inertial Response:* The transient energy variation of FAESS ( $\Delta E_{fa,trans}$ ) can be calculated by (18), where  $J_{fa}$  is the inertia value,  $f_{nom}$  and  $f_{nadir}$  are, respectively, the nominal and nadir frequency.

$$\begin{aligned} \Delta E_{fa,trans} &= J_{fa}(f_{nom}^2 - f_{nadir}^2)/2 \\ &\approx J_{fa}f_{nom}(f_{nom} - f_{nadir}) \\ &= J_{fa}f_{nom}\Delta f_{max} = J_{fa}f_{nom}^2 \frac{\Delta f_{max}}{f_{nom}} \\ &= H_{fa}S_{nom} \frac{\Delta f_{max}}{f_{nom}}. \end{aligned} \quad (18)$$

For transient analysis, the secondary frequency control in Fig. 10 is ignored. To create a second-order system, the total time constant of virtual governor is approximated by  $T_{gt} = \sqrt{T_{sg}T_{sa}}$  since  $T_{sg}$  and  $T_{sa}$  are close in amplitude. If  $T_{sa}$  is much smaller than  $T_{sg}$ , for example in FFR, the virtual governor effect should be included in the total damping block. Denoting the total inertia, damping, and governor gain as  $H_t = H_{fa} + H_{sg}$ ,  $D_t = D_{fa} + D_{sg}$ ,  $k_{pt} = k_{p,sg} + k_{p,sa}$ , respectively, the frequency dynamics can

TABLE I  
PARAMETERS AND VALUES OF THE TESTED SYSTEM

Parameters	Values	Parameters	Values
$f_{ref}$	60 Hz	$H_{sg}$	1.25 s
Power rating of FAESS	1 p.u.	$D_{sg}$	0
Energy capacity of FAESS	6.8 p.u.·s	$k_{p,sg}$	20
SoC <sub>ref</sub> of FAESS	0.5	$k_{i,sg}$	10
Power rating of SAESS	1 p.u.	$T_{sg}$	0.3 s
Power rating of SG	1 p.u.	$k_{p,sa}$	30
$D_{fa}$	10 p.u.	$T_{sa}$	0.1 s
$H_{fa}$	5 s	$k_{p,e}$	0.6
$T_h$	0.1	$k_{i,e}$	0.014

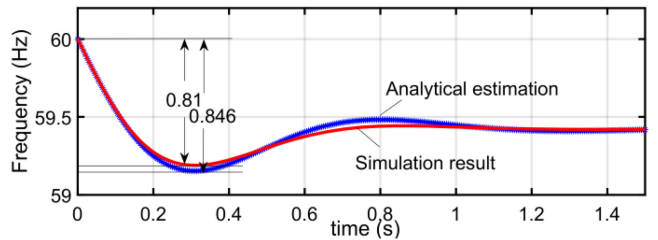


Fig. 11. Transient frequency due to 0.5 p.u. load increase for  $H_{fa} = 5$  s and  $D_{fa} = 2$  p.u.

be analytically solved by inverse Laplace transformation of the closed-loop transfer function, as written by

$$f(t) = f_{ref} \left( 1 - \frac{\Delta P_L}{k_{pt} + D_t} (1 - 2A_m e^{-\beta t} \cos(\Omega t + \varphi)) \right) \quad (19)$$

where the relevant parameters are given by

$$\begin{aligned} A_m &= \frac{\sqrt{k_{pt}(k_{pt}+D_t)}}{2\Omega H_t}, \\ \varphi &= \arctan \left( \frac{1}{\Omega} \left( \left( \frac{k_{pt} + D_t}{H_t} \right) - \beta \right) \right) \\ \beta &= (1/T_{gt} + D_t/H_t)/2, \Omega = \sqrt{k_{pe}/(H_t T_{gt}) - \beta^2}. \end{aligned} \quad (20)$$

The frequency nadir ( $f_{nadir}$ ) can be calculated at  $t_{nadir}$ , or the peak time of step response, as written as follows:

$$f_{nadir} = f(t_{nadir}), t_{nadir} = \frac{1}{\Omega} \arctan \left( \frac{2H_t T_{gt} \Omega}{D_t T_{gt} - H_t} \right). \quad (21)$$

For the parameters in Table I ( $D_{fa}$  is 2 p.u. to emphasize the inertial effect), the frequency response after 0.5 p.u. load increase based on the above-mentioned analysis is very close to the simulation result, as shown in Fig. 11. The maximum transient energy variation is  $\Delta E_{fa,trans} = H_{fa}S_{nom}(\Delta f_{max}/f_{nom}) = 0.07$  p.u.·s.

2) *Steady-State Energy Variation of ESS Due to Damping:* According to the final-value theorem, the steady-state energy variation of FAESS ( $\Delta E_{fa,ss}$ ) and SAESS ( $\Delta E_{sa,ss}$ ) due to power disturbance  $\Delta P_L$ , can be estimated by

$$\Delta E_{fa,ss} = \lim_{s \rightarrow 0} s \Delta E_{fa}(s) = \Delta P_{fa}(s)|_{s \rightarrow 0} = (D_{fa}/k_{i,sg}) \Delta P_L$$

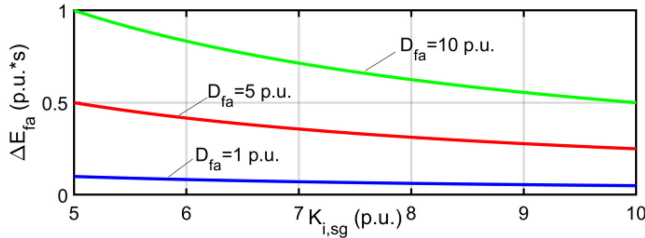


Fig. 12. Steady-state energy variation of FAESS due to 0.5 p.u. load increase, for different integral gain  $k_{i,sg}$  and virtual damping value  $D_{fa}$ .

$$\Delta E_{sa,ss} = \lim_{s \rightarrow 0} s\Delta E_{sa}(s) = \Delta P_{sa}(s)|_{s \rightarrow 0} = (k_{p,sa}/k_{i,sg})\Delta P_L \quad (22)$$

For SAESS, the mature and cheap energy-type storage such as lead-acid battery can be adopted, based on long-time energy and economy analysis. As seen from (22), the steady-state energy variation of FAESS is proportional to its damping term  $D_{fa}$  while reciprocal to the integral gain of the synchronous generator  $k_{i,sg}$ . For a 0.5 p.u. load increase, the variation  $\Delta E_{fa,ss}$  with respect to  $D_{fa}$  and  $k_{i,sg}$  is illustrated in Fig. 12. The following implications for system operation can be made.

- 1) If FAESS is adopted to provide damping support, there will be energy deviation in steady state, which will affect the external voltage of storage and reduces its cycle life.
- 2) With more synchronous generators retired from power system and, thus, smaller integral frequency control gain, FAESS will have larger energy variation for the same damping.

3) *Dynamic Energy Variation of FAESS:* For more accurate estimation, the dynamic energy variation  $\Delta E_{fa}$  in frequency domain is obtained in (23) whose inverse Laplace transformation yields the time-domain response

$$\Delta E_{fa}(s) = \frac{\Delta P_{fa}(s)/s}{(T_{sg}s+1)(T_{sa}s+1)(H_{fa}s+D_{fa})\Delta P_L} = \frac{s\left\{((H_{sg}+H_{fa})s+D_{sg}+D_{fa})(T_{sg}s+1)(T_{sa}s+1)s + (k_{p,sa}s)(T_{sg}s+1) + (k_{p,sg}s+k_{i,sg})(T_{sa}s+1)(T_h s+1)\right\}}{(T_{sg}s+1)(T_{sa}s+1)(H_{fa}s+D_{fa})\Delta P_L} \quad (23)$$

For a 0.5 p.u. load increase, the dynamic energy variation of FAESS is depicted in Fig. 13. A mapping relationship between different inertia/damping and the corresponding energy variation can be obtained. The solid lines indicate the critical damping values beyond which the energy dissipated in the damping support will be larger than in the inertial support.

4) *Sizing of FAESS Based on Maximum Energy Variation:* It is also observed Fig. 13 that the maximum energy variation of FAESS in the whole process is determined by

$$\Delta E_{max} = \max \{ \Delta E_{fa,trans}, \Delta E_{fa,ss} \}. \quad (24)$$

For instance, if  $H_{fa}$  and  $D_{fa}$  are selected as 5 s and 1.6 p.u., based on the analytical calculation above or the curves in Fig. 13,  $\Delta E_{fa,trans}$  and  $\Delta E_{fa,ss}$  are found to be 0.07 p.u. $\cdot$ s and 0.08 p.u. $\cdot$ s, respectively. The maximum energy variation is  $\Delta E_{max} = 0.08$  p.u. $\cdot$ s. If the energy variation proportion is

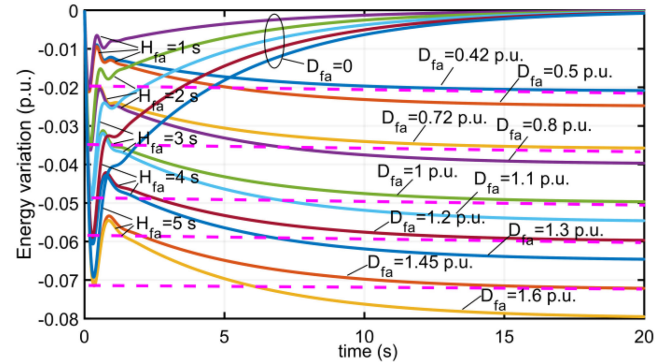


Fig. 13. Energy variation of FAESS due to 0.5 p.u. load increase for different inertia  $H_{fa}$  and damping  $D_{fa}$ .

$\Delta E\%_{max,allowed} = 10\%$ , the energy capacity of FAESS will be 0.8 p.u. $\cdot$ s.

On the other hand, if we consider the case that energy from inertia is larger, equating (17) with (18) yields the nominal energy  $E_{nom}$  for FAESS to synthesize the given inertia value, as formulated by

$$E_{nom} = H_{fa}S_{nom} \left( \frac{\Delta f_{max}}{f_{nom}} \right) / \Delta E\%_{max,allowed} = E_{kin} \frac{\Delta f_{max}\%}{\Delta E\%_{max,allowed}} \quad (25)$$

which indicates  $E_{nom}$  is equal to the equivalent kinetic energy ( $E_{kin}$ ) multiplied by the ratio between maximum frequency variation percentage and allowable energy variation percentage.

In (25),  $\Delta f_{max}$  can be obtained by estimation or grid-code requirement, and the value of  $H_{fa}$  can be designed as per the desired frequency performance, such as the largest deviation or RoCoF. Since the energy variation range of FAESS can be much wider than the frequency variation range,  $E_{nom}$  can be much smaller than the kinetic energy from conventional synchronous generator for identical inertia value. For instance, if  $\Delta f_{max} = 5\%$  and  $\Delta E\%_{max,allowed} = 10\%$ , the energy of FAESS is half the conventional kinetic energy.

The maximum allowable energy variation percentage  $\Delta E\%_{max,allowed}$  depends on the energy characteristics of FAESS. Taking the dc-side capacitor as an example,  $\Delta E\%_{max,allowed}$  can be calculated by

$$\Delta E\%_{max,allowed} = \frac{(CV_{dc,nom}^2 - CV_{dc,min}^2)/2}{CV_{dc,nom}^2/2} \approx \frac{2\Delta V_{dc,max}}{V_{dc,nom}}. \quad (26)$$

Assuming 10% maximum dc voltage deviation and  $\Delta f_{max}\% = 5\%$ , for a system with  $S_{nom} = 360$  kVA and  $V_{dc,nom} = 600$  V, to synthesize  $H_{fa} = 5$  s, the dc capacitance ( $C$ ) is 2.5 F based on (25) and (26), which is too large for the conventional dc capacitor designed to reduce current and voltage ripple.

Given the losses and long-term degradation of storage, and stability margin in various scenarios, FAESS should be slightly oversized. For a FAESS with 6.8 p.u. $\cdot$ s, it can synthesize an inertia as large as  $H_{fa} = 13.6$  s for 5% frequency and 10% SoC

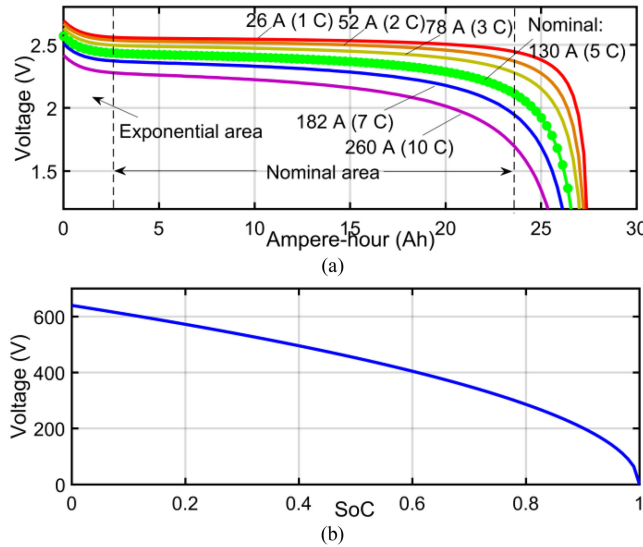


Fig. 14. Discharge characteristics of energy storage. (a) Voltage and Ampere-hour relation of a titanate battery cell at different C rates. (b) Voltage and SoC relation of supercapacitor with  $V_{dc,nom} = 640$  V and  $C = 2.9$  F [49].

variation according to (25). The parameters of the testbed in Fig. 6 are summarized in Table I. For a more general study, the voltage and power levels are not specified.

#### D. Effect of Storage Characteristics and Management

1) *Voltage-Energy Characteristics*: The above-mentioned analysis gives a lower-bound estimation of the energy capacity of FAESS. The practical storage selection should also consider the physical constraints such as C rate and single cell parameters. For example, assuming 0.5 p.u. power disturbance, for a battery storage with a C-rate at 5 C, the energy capacity will be 0.1 p.u. $\cdot$ h, which is much larger than 6.8 p.u. $\cdot$ s as calculated previously. If the base power of a practical power system is 300 kVA and the dc voltage is 600 V, then the energy capacity of FAESS will be 30 kWh. For the 2.4 V/26 Ah lithium titanate battery cell [48], the required battery pack can be realized by assembling 240 cells in series and then having two groups in parallel.

Practical energy storage operation should also consider the nonlinear characteristics, which will be reflected by the voltage variation as the stored energy changes. For the selected lithium titanate battery, the relation of SoC and voltage ( $E_{ess}$ ) can be expressed by (27). The  $SoC_{ess}(t_0)$  is the initial SoC when storage is used, which can be determined by open-circuit voltage method,  $\eta$  is the power conversion efficiency. The discharge curve of the battery cell in Fig. 14(a) indicates that the internal voltage keeps almost constant and linear in the middle SoC range (15%–85%), especially for small C rate. The curve is exponential in high SoC range. The 0.15 SoC change will result in 0.1 V voltage change (4%), but the voltage change is still slow. For a C rate at 5 C, such voltage variation will take place in 1.8 min. The voltage may drop rapidly near cutoff voltage in small SoC range. However, this range should normally be forbidden by battery management system

$$\begin{aligned} SoC_{ess}(t) &= SoC_{ess}(t_0) - \int_{t_0}^t P_{ess}/\eta dt \\ E_{ess}(t) &= f(i_{ess}, SoC_{ess}). \end{aligned} \quad (27)$$

Based on the SoC calculation in (28), the voltage of supercapacitor ( $V(t)$ ) decreases more drastically as the stored charge drains, as illustrated in Fig. 14(b), [49]. Therefore, to guarantee an acceptable voltage for power converter operation, for example 10%, a timely energy recovery is mandatory

$$SoC_{ess}(t) = C(V(t)/V_{dc,nom})^2. \quad (28)$$

For a double-stage ESS, the nonideal storage characteristics can be eliminated by dc converters with fixed output voltage control. For a single-stage ESS, the dc voltage discrepancy will not affect the equivalent current or voltage source determined by closed-loop control of the ac converter if the modulation index is within the normal range. Therefore, the nonlinear effect will be invisible on the grid side, thus ensuring isolation between ac grid side and the storage side. This also provides the feasibility to study the dynamics of VSM and energy storage separately. VSM can be physically validated by a hardware converter with constant dc voltage while ESS and DC PCS can be emulated by software, which is also the principle of hardware test in Section V.

2) *Effect of Battery Management System (BMS)*: The error and delay in SoC estimation may happen in practice, especially when there is rapid current variation, which will affect the accuracy of SoC control. However, as discussed previously, the effect of such error on VSM will be compensated by closed-loop control. Moreover, the variation SoC is so slow, usually in a second-to-minute time scale, that the dc voltage of the VSM converter can be treated as constant for the voltage and current control loop (ms scale). Other BMS functions such as battery cell balancing within the storage pack will not affect the external performance of VSM.

## IV. VSM PARAMETERS AND CONTROL LOOP DESIGN

### A. Control Design of VSM Parameters

1) *Small-Signal Stability Analysis*: According to the conventional grid code on inertial requirement and the emerging VSM standard [18], the initial recommended value of inertia (5–12 s) and damping (10 p.u.) value of the VSM parameters are selected. However, for a specific power network, a more dedicated design is still needed to ensure the inertia and damping value can meet the small-signal stability requirement.

An analytical expression of the oscillation modes will be difficult to obtain for a multiple-machine system, though an effort for multiple VSM analysis was made by our previous research work [21]. The linearization toolbox of MATLAB/Simulink is adopted to carry out the stability or oscillation analysis, with even higher accuracy and simplicity. The control parameters ensuring desirable dynamics, including  $H_{fa}$ ,  $D_{fa}$ , and  $T_h$ , are obtained by eigenvalue analysis.

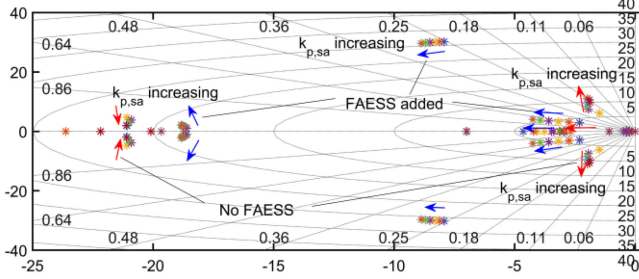


Fig. 15. Root locus with  $k_{p,sa}$  increasing from 5 to 30, before (red) and after (blue) adding FAESS with  $H_{fa} = 5$  s,  $D_{fa} = 10$  p.u., and  $T_h = 0.1$ .

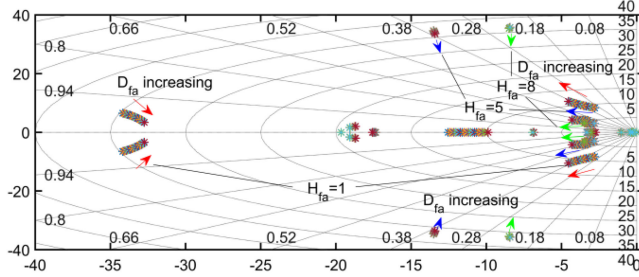


Fig. 16. Root locus as  $D_{fa}$  increases from 0.5 to 10.5 p.u., for  $H_{fa} = 1$  s (red), 5 s (blue), 8 s (green), respectively, and  $T_h = 0.1$ .

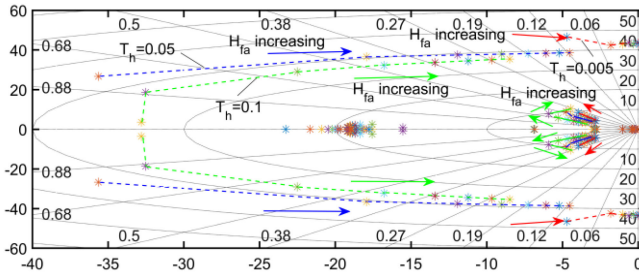


Fig. 17. Root locus as  $H_{fa}$  increases from 1 s to 8 s, for  $H_{fa}/D_{fa} = 0.5$  and  $T_h = 0.005$  (red), 0.05 (blue), and 0.1 (green), respectively.

The effect of FAESS on improving system stability is exhibited in Fig. 15 where the root locus for increased  $k_{p,sa}$  is displayed. Damping ratio of the dominant mode close to right-half-plane is significantly increased after adding FAESS with proper  $H_{fa}$  and  $D_{fa}$ . However, another mode at around 30 rad/s is introduced, which is interoscillation between FAESS and SG due to the mismatched ratio of inertia and impedance, as analytically discussed in [21]. As illustrated in Fig. 16, for constant  $H_{fa}$ , the dominant modes will move leftwards as  $D_{fa}$  increases, indicating an enhanced damping ratio. Another crucial factor in oscillation mitigation is the leading term  $T_h s$ . It is revealed in [21] that tuning  $H_{fa}$  and  $D_{fa}$  solely cannot mitigate the oscillation modes near and below the synchronous frequency of a single VSM, and interoscillation modes between VSMs. Instead, a small  $T_h$  can dampen all the modes and improve stability, as demonstrated in Fig. 17. However, a large  $T_h$  will countervail the inertia effect.

2) *Bandwidth Separation in Frequency Control:* Ignoring the time delay in governor control, the simplified model of the

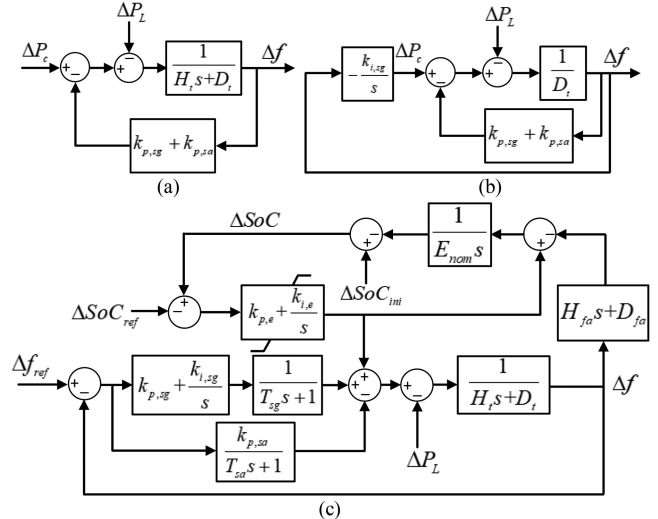


Fig. 18. Diagram of frequency control of the system. (a) Simplified primary control. (b) Simplified secondary control. (c) Detailed control integrated with SoC recovery of FAESS.

primary control loop is presented in Fig. 18(a). Therefore, its bandwidth ( $\omega_{bw,primary}$ ) can be approximated by

$$\omega_{bw,primary} = \frac{k_{p,sg} + k_{p,sa} + D_{sg} + D_{fa}}{H_{fa} + H_{sg}}. \quad (29)$$

For secondary frequency control, since its bandwidth should be much lower than the primary control loop, its model can be simplified, as Fig. 18(b), with  $s = 0$  in the inner loop [50]. Its bandwidth ( $\omega_{bw,secondary}$ ), which is also the bandwidth of the load disturbance transfer function is estimated as

$$\omega_{bw,secondary} = \frac{k_{p,sg}}{k_{p,sg} + k_{p,sa} + D_{sg} + D_{fa}}. \quad (30)$$

## B. Energy Recovery Control Design

Once the inertial and damping parameters of VSM are selected, the size of FAESS can be determined based on the analysis in Section III. A SoC control loop is added to recover the energy of FAESS. The detailed frequency control model considering energy recovery control is given in Fig. 18(c).

1) *Design of Proportional Gain:* As the outermost loop, the bandwidth of SoC control  $G_e(s)$  should be lower than that of SoC recovery control to alleviate its impact on inertia-damping response and frequency regulation, as illustrated in Fig. 18(c). The SoC recovery control loop can then be transformed into Fig. 19(a) where the effect of frequency control appears in the disturbance from load and the inner power control loop, as quantified by  $G_f(s)$  in (10). Letting  $s = 0$  in the inner control loop, the SoC control loop can be further simplified as Fig. 19(b). Since the control plant is an integral block, a proportional block should normally be able to obtain zero steady-state error. The bandwidth of the simplified SoC control loop is then given by

$$\omega_{bw,SoC} = k_{p,e}/E_{nom}. \quad (31)$$

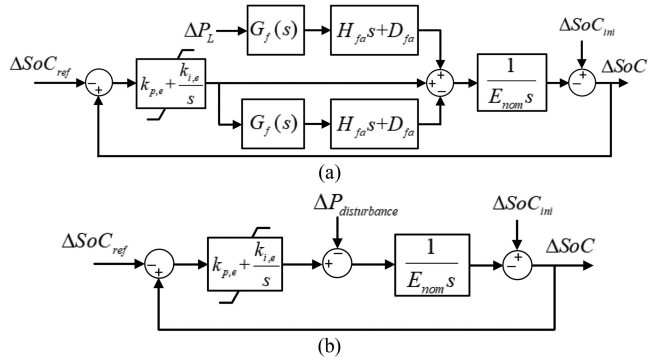


Fig. 19. Diagram of SoC recovery control. (a) Considering load disturbance and frequency control. (b) Simplified mode.

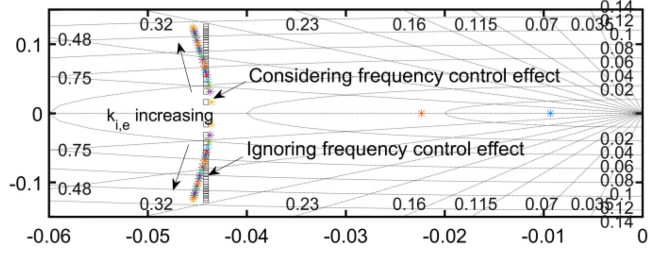


Fig. 20. Root locus of SoC control loop with  $k_{i,e}$  varying from 0.005 to 0.05.

The larger value of  $k_{p,e}$  can achieve faster energy recovery, but may lead to control loop interference and thus frequency performance deterioration, or even severe stability issues. If the SoC control loop is included in the power reference of FAESS, the practical frequency deviation of FAESS is found to be

$$-\frac{1}{H_{fa}s + D_{fa}} \left( -\Delta P_{fa} \frac{k_{p,e}}{E_{m}s} - \Delta P_{fa} \right) = -\Delta f. \quad (32)$$

By organizing the blocks and inverse Laplace transformation, the effective inertia and damping of FAESS are roughly approximated by

$$H_{fa,eff} = H_{fa} e^{-(k_{p,e}/E_{nom})t}, D_{fa,eff} = D_{fa} e^{-(k_{p,e}/E_{nom})t} \quad (33)$$

which will decay more rapidly as  $k_{p,e}$  increases. Therefore, it can be concluded that fast SoC recovery will counteract the virtual inertia and damping control, which also reflects the physical meaning and cost of control loop overlapping.

2) *Design of Integral Gain:* Considering the parasitic losses of storage and the absence of frequency integral control in peer-to-peer controlled systems, an additional integral block may also be added in the SoC recovery control loop. The SoC control loop will then be in the form of a second-order system with the tendency to oscillate, for which the integral gain should be carefully tuned. In Fig. 21,  $k_{p,e}$  is 0.6, and  $k_{i,e}$  increases from 0.005 to 0.05 with granularity at 0.005. For the simplified system in Fig. 19(b), the real part of the root is kept constant while the imaginary part increases monotonically, which is close to the roots obtained from the detailed model, as shown in Fig. 20. To

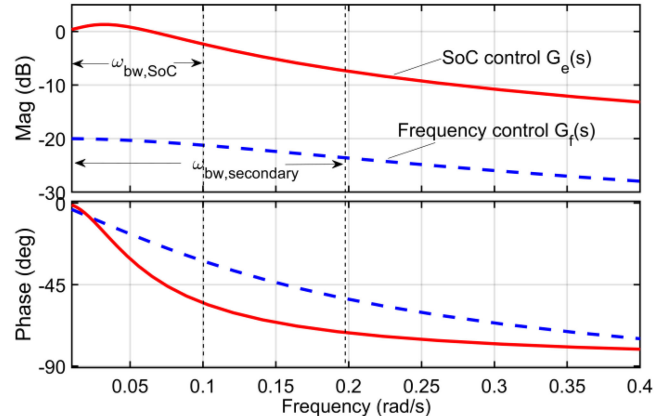


Fig. 21. Bode plots of the frequency control loop ( $G_f$ ) and the SoC recovery control loop ( $G_e$ ).

TABLE II  
BANDWIDTH OF THE CONTROL LOOPS

Control loop	Symbol	Analytical	Bode plot
Primary frequency	$\omega_{bw,primary}$	9.6 rad/s	8.5 rad/s
Secondary frequency	$\omega_{bw,secondary}$	0.17 rad/s	0.19 rad/s
SoC recovery	$\omega_{bw,SoC}$	0.09 rad/s	0.1 rad/s

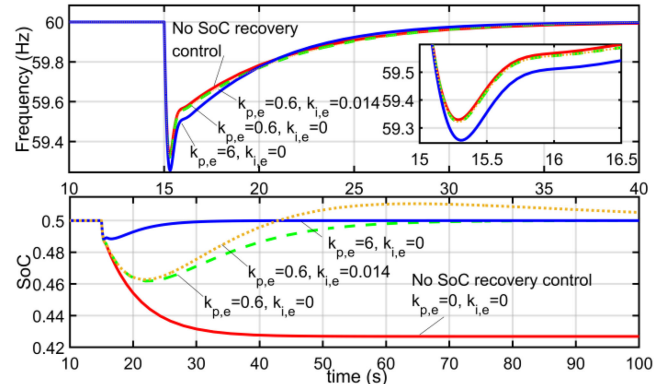


Fig. 22. Frequency and SoC dynamics for different SoC control options.

ensure proper damping and keep the original bandwidth, a small  $k_{i,e}$  (0.014) is selected, with damping ratio of the system near 0.8. In this way, the performance of the overall SoC PI control loop can still be treated similar to the original proportional control loop.

For the selected value  $k_{p,e} = 0.6$  and other parameters in Table I, the estimated bandwidth of the three control loops based on the above analysis are listed in Table II, which clearly obeys the bandwidth separation rule. Those values obtained from the Bode plots of  $G_e(s)$  and  $G_f(s)$  also closely matches the analytical calculation, as illustrated in Fig. 21.

3) *Time-Domain Verification:* The above-mentioned analysis is also verified by time-domain results of the simplified model. For the studied system, the SoC and frequency performance for different SoC recovery control are presented in Fig. 22. Without SoC recovery control, there is a 0.73 SoC

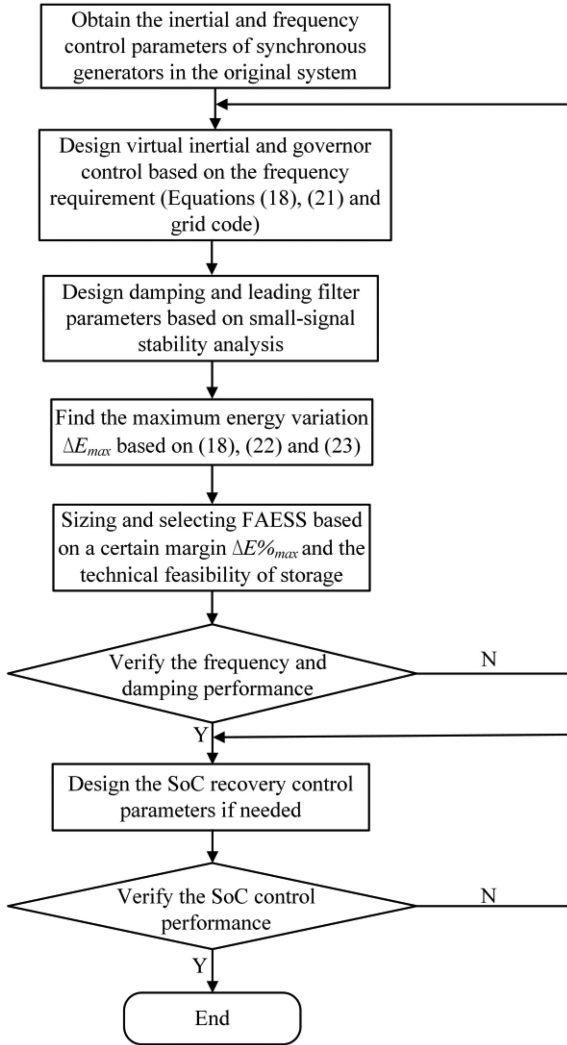


Fig. 23. Complete process of VSM control design and FAESS sizing.

drop. The frequency is regulated the best among others. With the designed proportional control ( $k_{p,e} = 0.6$ ,  $k_{i,e} = 0$ ), the frequency performance behaves similarly and SoC gets recovered. For large  $k_{p,e} = 6$ , SoC gets recovered very rapidly but has larger frequency deviation. Small SoC integral gain ( $k_{i,e} = 0.014$ ) has a trivial effect on frequency dynamics but introduces a small oscillation in the energy recovery process.

### C. Complete Procedure of VSM Design

The complete procedure of designing VSM is sketched by Fig. 23 and briefly explained as follows. First, the initial values of virtual inertia and governor parameters are selected based on frequency regulation requirement. After that, these parameters will be adjusted by small-signal stability analysis and bandwidth separation. The FAESS will then be sized based on the inertia and damping parameters, as done in Section III.

Additional SoC recovery control loop will, then, be designed based on bandwidth and stability constraints. The SAESS will be selected by the long-term energy management requirement,

usually with an energy capacity at one-to-two per-unit hour. Finally, simulation and hardware test will be carried out to verify the VSM control and modify the parameters if necessary.

## V. OFFLINE VERIFICATION OF VSM CONTROL WITH PRACTICAL ENERGY STORAGE MODEL

Both dc and ac coupled schemes are presented here, with FAESS adopting lithium titanate battery and supercapacitor respectively, to examine the nonlinear effect of energy storage. The SAESS model uses an ordinary lead-acid battery. As the research is focused on energy recovery control, fixed parameters  $H_{fa} = 10$  s,  $D_{fa} = 10$  p.u. are implemented on VSM. The physical and control parameters for both schemes are listed in Tables I and IV. Switched models of power converters are adopted, with switching frequency at 10 kHz.

### A. DC-Coupled ESS Using Lithium Titanate Battery

First, lithium titanate battery with the discharge curve in Fig. 14(a) is selected as the FAESS. A 0.5 p.u. load increase occurs at  $t = 15$  s. For initial SoC set around 0.5, the waveforms of power, frequency and SoC are shown in Fig. 24(a). The frequency nadir is 59.5 Hz at  $t = 15.5$  s. The power of dc filter capacitor is trivial compared to the power provided by ESS. For a different initial SoC such as 0.15, the power and frequency dynamics, and the variation of SoC are almost identical, as shown in Fig. 24(b). This demonstrates that the VSM performance is independent of the nonlinear SoC-voltage characteristics at different SoC and voltage levels. The terminal voltage of the FAESS undergoes 20 V drop (3.2%) due to the internal series resistor ( $0.096 \Omega$ ) and soon restores. The steady-state variation of SoC (0.1%) and voltage after inertial response are very small, which will not affect the continuous operation.

Therefore, for FAESS with relatively large energy capacity, the energy recovery control is not so urgent. Instead, the SoC can be managed by a higher-level energy management system, such as the rule-based dispatch strategy presented in [51].

### B. DC-Coupled ESS Using Supercapacitor

A case with supercapacitor in Fig. 14(b), as FAESS is tested. As shown in Fig. 25(a) and (b), regardless of SoC recovery control, the active power and frequency performance are almost identical to the case of lithium titanate battery. Without SoC recovery, the SoC variation is close to the analytical estimation by (22), or  $(D_{fa}/k_{i,sq} \cdot \Delta P_L)/E_{nom} = (10/10 \cdot 0.5)/6.8 = 7.35\%$ , which also matches the energy variation of FAESS in Fig. 13, or  $(0.08 \text{ p.u.} \cdot \text{s}) \cdot (10/1.6)/(6.8 \text{ p.u.} \cdot \text{s}) = 7.35\%$ . This makes the dc voltage of the supercapacitor drop to 620 V, which may result in abnormal modulation.

As demonstrated, the proportion of energy variation of supercapacitor in VSM control may be outstanding, so an immediate energy recovery is needed. It is shown in Fig. 25(b) that with SoC recovery control, the frequency and power performance is almost unchanged, while the SoC will be recovered. The dc voltage of the supercapacitor in the two cases are shown in Fig. 25(c). The transient voltage drop is due to the internal resistance of

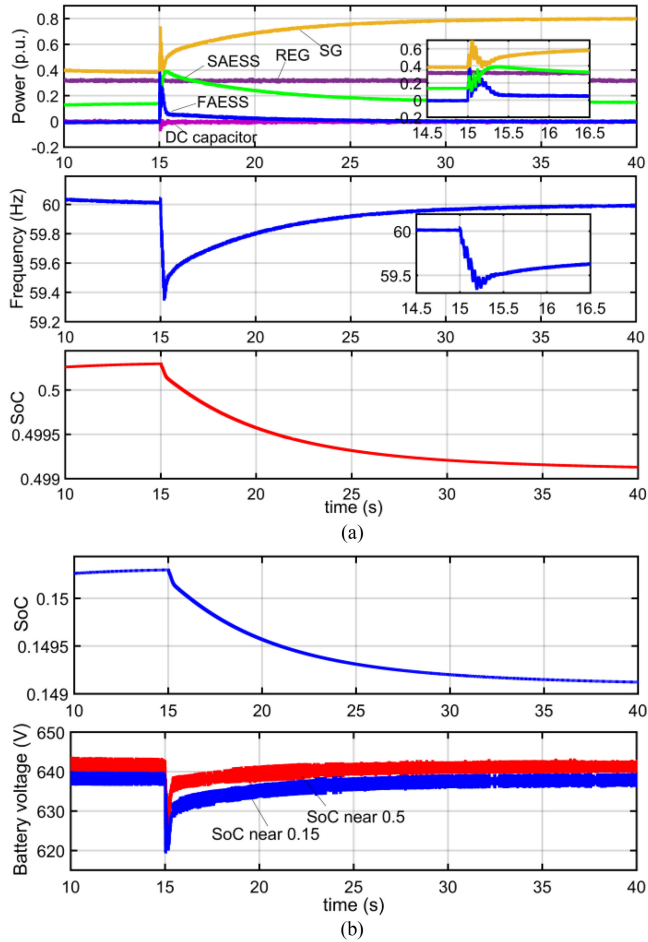


Fig. 24. Simulation results of VSM ( $H_{fa} = 10$  s and  $D_{fa} = 10$  p.u.) in dc-coupled scheme with Lithium Titanate battery. (a) Active power, frequency, and SoC, with initial SoC of FAESS at around 0.5. (b) SoC variation around 0.15, voltage variation for SoC near 0.15 and 0.5.

the supercapacitor, while the steady-state variation is due to the provided damping.

### C. AC-Coupled ESS With Delay in SoC Measurement

This case tests the ac coupled ESS, with SAESS and supercapacitor connected directly to the dc side of the ac–dc converter. As seen in Fig. 26, the behaviors of active power, frequency and SoC are the same as the dc-coupled case. To study the effect of BMS on dynamic performance, a delay is artificially added in SoC measurement. However, as seen, such delay has a negligible effect on the power and frequency performance, but a slight difference in the SoC recovery, even for a long delay of 5 s. The SoC of FAESS in the three conditions is controlled equal in a ten-second time scale.

## VI. REAL-TIME TESTING RESULTS

For the convenience of implementation in an all-power-electronic-converter-based test bench, the rotational SG is emulated by a power electronic converter based on the same principle of VSM. For ESS, its SoC variation is calculated by integrating

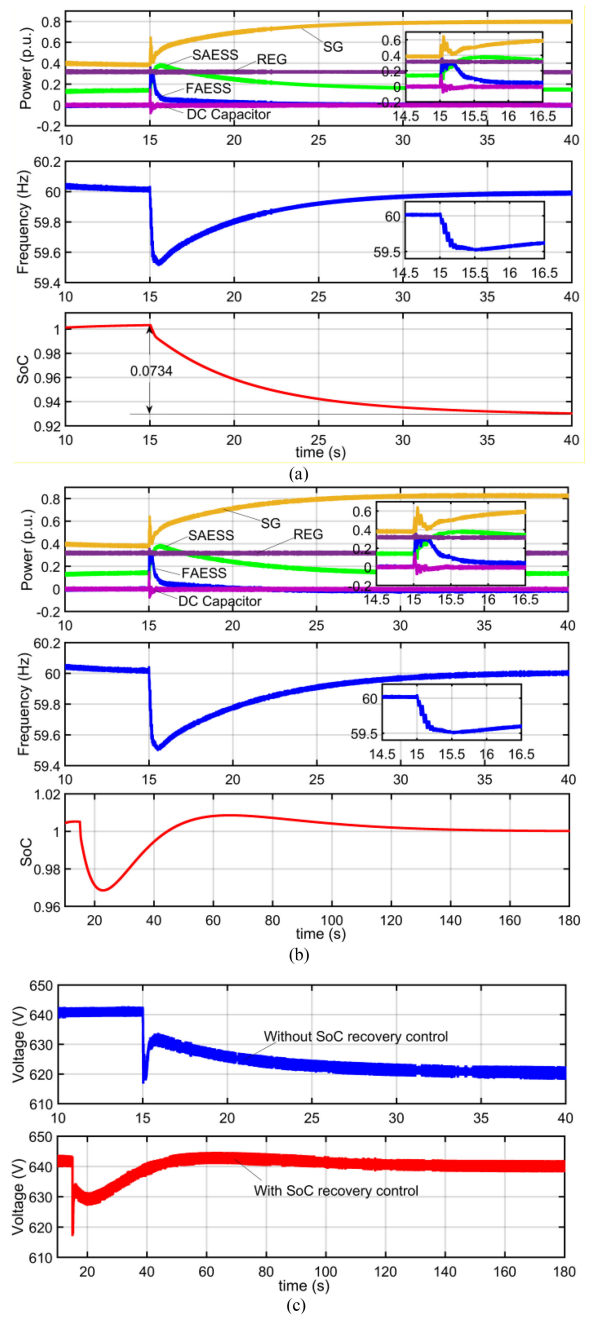


Fig. 25. Simulation results of VSM ( $H_{fa} = 10$  s and  $D_{fa} = 10$  p.u.) in dc-coupled scheme with FAESS being supercapacitor. (a) Power, frequency, and SoC performance without SoC recovery control. (b) Power, frequency, and SoC performance with SoC recovery control. (c) DC voltage of supercapacitor without and with SoC recovery control.

active power and dividing the energy capacity. A real-time simulator is used as the controller in the rapid control prototype (RCP) test, which receives current and voltage signals and sending PWM signals to the power converters. The schematic diagram of the hardware testbench is depicted in Fig. 27 and the parameters are given in Table III. The voltage and power levels are scaled down for secure testing in the laboratory, but can also be extended to high power levels.

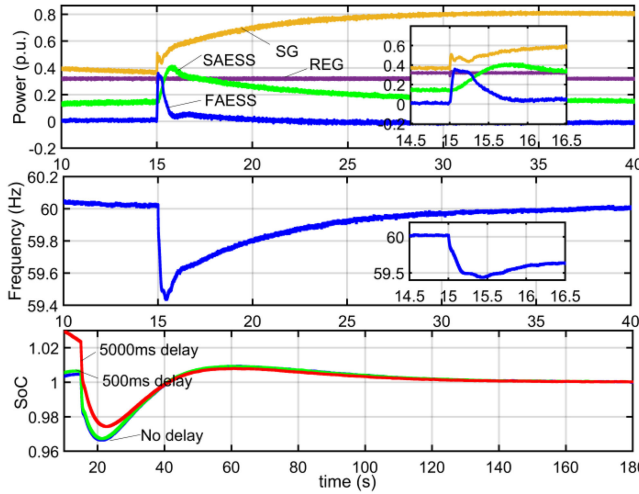


Fig. 26. Simulation results of VSM ( $H_{fa} = 10$  s and  $D_{fa} = 10$  p.u.) in ac-coupled scheme, with SoC recovery control and different delay time in measuring the SoC of FAESS.

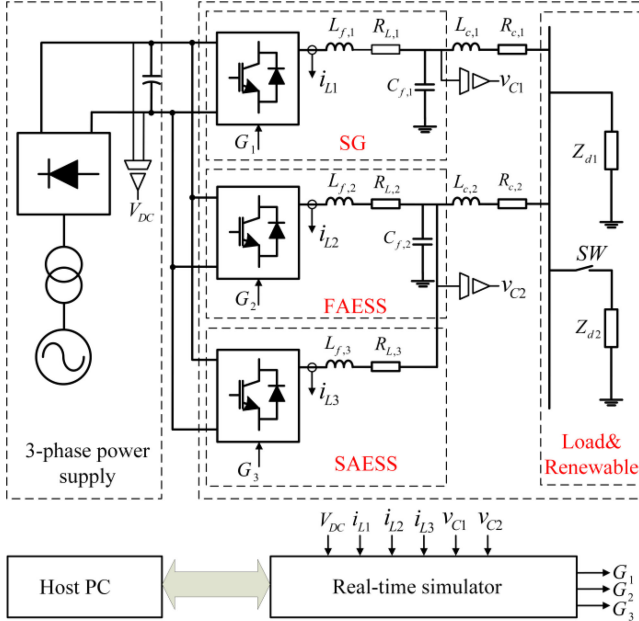


Fig. 27. Schematic diagram of the hardware testbed.

TABLE III  
PARAMETERS AND VALUES OF THE RCP TEST BENCH

Parameters	Values	Parameters	Values
Base power ( $S_b$ )	220 VA	$Z_{d1}$	2 p.u.
$f_{ref}$	60 Hz	$Z_{d2}$	2 p.u.
$V_{dc}$	155 V	$L_{f1}$	0.175 p.u.
$V_{ac}(LL)$	49 V	$R_{f1}$	0.046 p.u.
Power rating of FAESS	1 p.u.	$C_{f1}$	0.083 p.u.
Energy capacity of FAESS	1500 Ws	$L_{c1}$	0.034 p.u.
SoC <sub>ref</sub> of FAESS	0.5	$R_{c1}$	0.033 p.u.
Power rating of SAESS	1 p.u.	$L_{f2}$	0.34 p.u.
Energy capacity of SAESS	220 Wh	$R_{f2}$	0.046 p.u.
Power rating of SG	1 p.u.	$C_{f2}$	0.083 p.u.
$L_{c2}$	0.034 p.u.	$R_{c2}$	0.033 p.u.
$L_{f3}$	0.5 p.u.	$R_{L3}$	0.023 p.u.

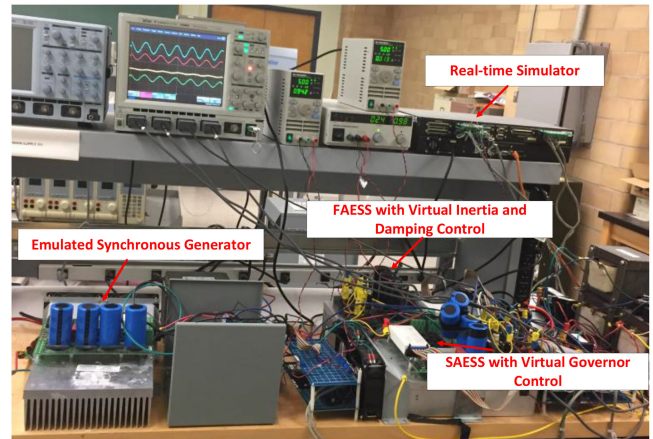


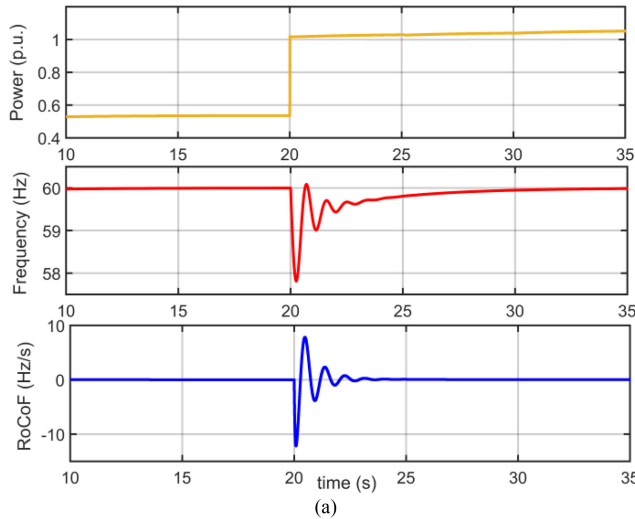
Fig. 28. Experimental setup of the hardware test bench.

All power converters adopt a three-phase two-level topology with switching frequency at 18 kHz, which are controlled with a real-time simulator whose simulation step is fixed at 20  $\mu$ s. The three-phase resistive load  $Z_{d2}$  (22  $\Omega$ ) serves as a power disturbance as the switch (SW) turns ON or OFF. A photograph of the hardware test setup is shown in Fig. 28. The model of the network is first simulated offline and then compared with hardware RCP tests.

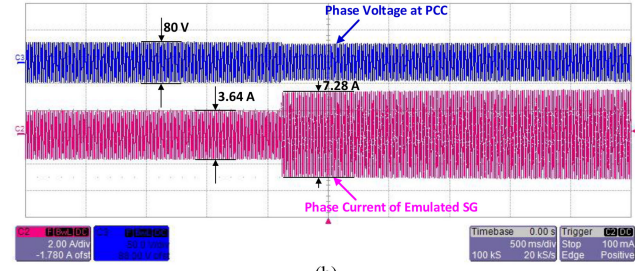
#### A. Case 1: Synchronous Generator Alone and With SAESS

This case study will first investigate the response of the synchronous generator alone when the load is increased from 0.5 to 1 p.u. as the SW gets closed. Fig. 29(a) presents the simulation results. Since the inertia of SG is small, the frequency nadir is 57.81 Hz at  $t = 20.26$  s, and the maximum RoCoF is around 10 Hz/s. As the load power will be solely supplied by the emulated SG, there is no oscillation in the current and power waveform. The swing in frequency waveform is relatively severe due to the low damping ratio from SG and its control. The hardware test results in Fig. 29(b) and (c) closely match the simulation results.

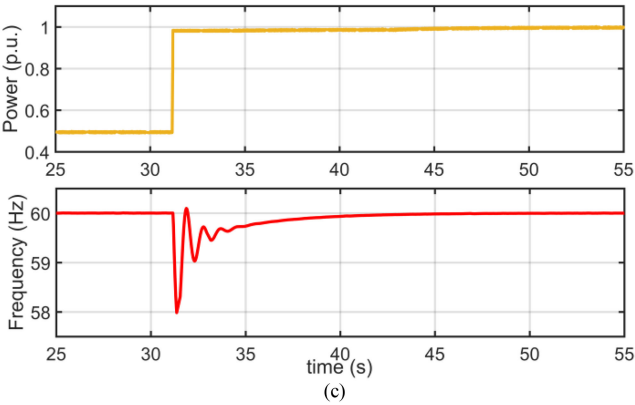
In Fig. 30, SAESS adopting virtual governor control is added in the system, with the initial power reference at 0.15 p.u. For the same load disturbance, the frequency performance is improved, with frequency nadir increased to 58.52 Hz at  $t = 20.15$  s. However, as the total droop gain of synchronous generator and SAESS increases, the transient oscillation becomes more severe, as exhibited in the current and power waveform of SG and SAESS. The oscillation frequency is measured to be 2 Hz, which is close to the dominant poles in Fig. 15. Notice that oscillation in Fig. 30(c) is slightly more severe than the simulation results in Fig. 30(a), possibly due to the nonlinear effect of PLL or the parameter mismatch between the practical devices and the simulated model. However, such distinction will not be so apparent when a FAESS with virtual inertia and governor control is added.



(a)



(b)



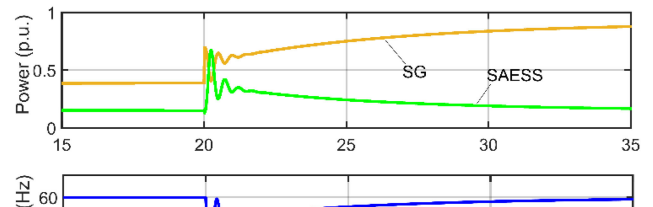
(c)

Fig. 29. Results for synchronous generator alone. (a) Power, frequency, and RoCoF from simulation. (b) Voltage and current waveform in the hardware test. (c) Power and frequency waveform in the hardware test.

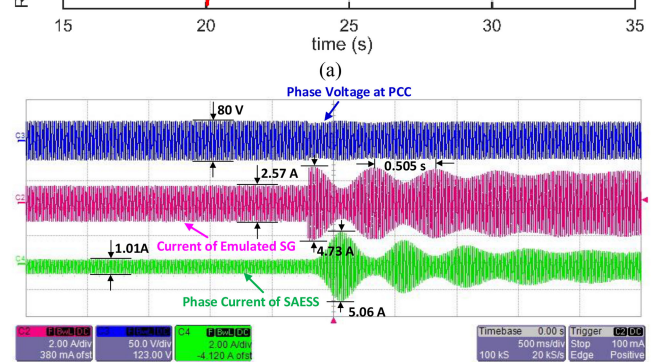
### B. Case 2: Add FAESS for Inertia-Damping Emulation

In this case, FAESS with inertia-damping emulation and virtual energy capacity of 6.8 p.u. $\cdot$ s is added in the system, but without energy recovery control. In Fig. 31, the parameters of FAESS are  $P_{ref,fa} = 0$ ,  $H_{fa} = 5$  s,  $D_{fa} = 10$  p.u., and  $T_h = 0.1$ . The frequency nadir is 59.19 Hz at  $t = 26.52$  s and RoCoF is 4 Hz/s.

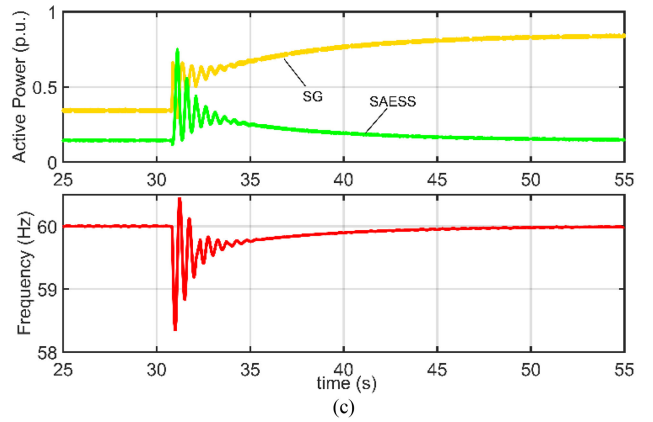
The power waveform of SAESS becomes less steep. However, the SoC of FAESS keeps dropping, as with conventional droop-controlled inverter or VSM. The SoC variation (6.85%) is slightly smaller than the simulation result (7.34%) in Fig. 25(a). This difference is because the actual power increment is less than 0.5 p.u. due to the voltage drop over feeder lines as the resistive



(a)



(b)



(c)

Fig. 30. Results for the case with SG and SAESS. (a) Power, frequency, and RoCoF from simulation. (b) Voltage and current waveform in the hardware test. (c) Power and frequency waveform in the hardware test.

load increases. The oscillation is significantly mitigated due to the inertia and damping control from FAESS.

Given the consistency of simulation results with hardware experimental results, only hardware test waveforms of power, frequency and SoC are presented in the following cases, without loss of valuable information.

### C. Case 3: With Varied Control Parameters

Since the inertia and damping of FAESS can be flexibly programmed, their impact on dynamic performance is further

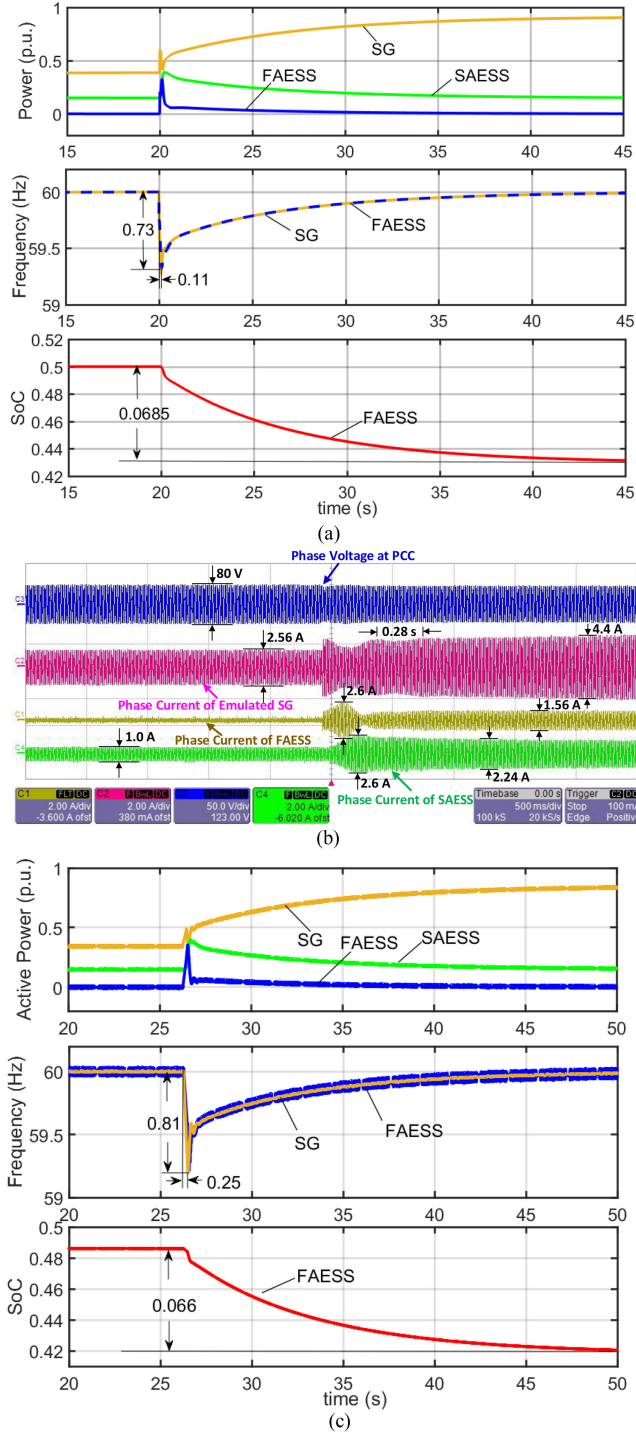


Fig. 31. Hardware test results for the case of adding FAESS with  $H_{fa} = 5$  s, and  $D_{fa} = 10$  p.u., but without SoC recovery control. (a) Power, frequency, and RoCoF from simulation. (b) Power, frequency, and SoC in hardware test. (c) Voltage and current waveform in the hardware test.

studied here. Because the conventional synchronous generator has fixed inertia and little damping, the VSM control can provide superior frequency control performance.

1) *With Increased Inertia  $H_{fa}$ :* As shown in Fig. 32, with increased inertia ( $H_{fa} = 10$  s), the frequency nadir rises to

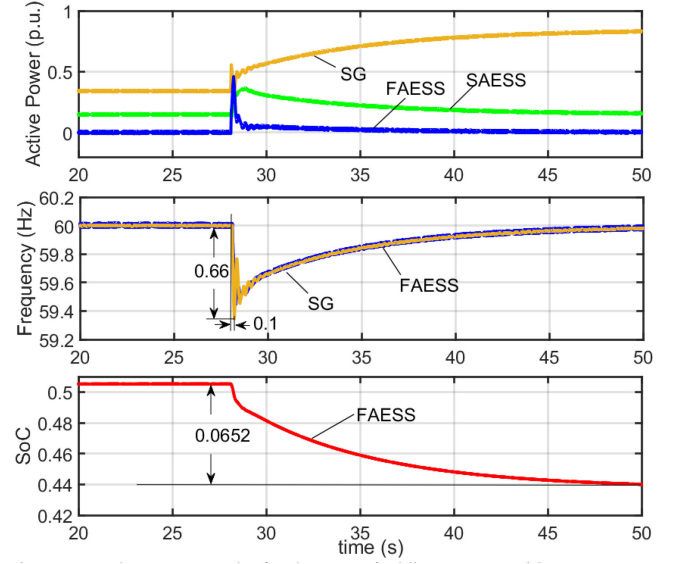


Fig. 32. Hardware test results for the case of adding FAESS with  $H_{fa} = 10$  s and  $D_{fa} = 10$  p.u., but without SoC recovery control.

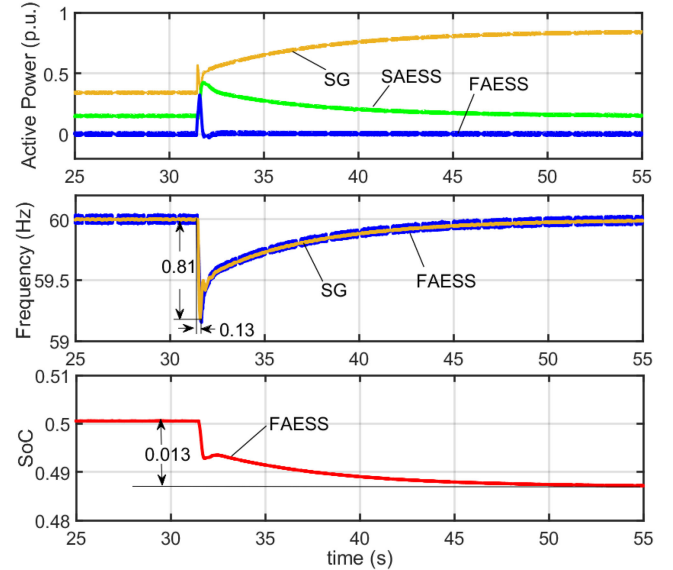


Fig. 33. Hardware test results for the case of adding FAESS with  $H_{fa} = 5$  s and  $D_{fa} = 2$  p.u., but without SoC recovery control.

59.34 Hz at  $t = 28.22$  s, with RoCoF drastically reduced. The power response of SAESS is also slowed down, while the steady-state SoC variation of FAESS is almost equal to the former case. However, the oscillation is slightly aggravated due to the decreased damping-to-inertia ratio, according to stability analysis in Fig. 16.

2) *With Smaller Damping  $D_{fa}$ :* Fig. 33 demonstrates that oscillation is worsened by a lower damping value ( $D_{fa} = 2$  p.u.). The frequency deviation and RoCoF are also worse than the larger damping case. However, the steady-state energy variation is smaller, which agrees with the implication in (22)

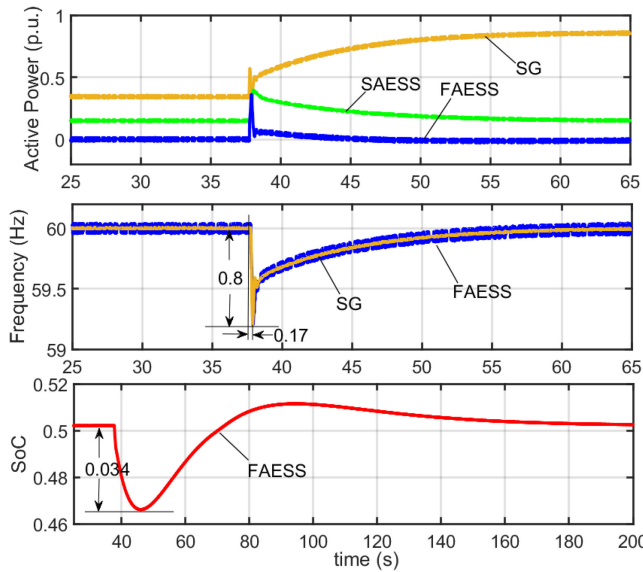


Fig. 34. Hardware test results for VSM ( $H_{fa} = 5$  s and  $D_{fa} = 10$  p.u.) with SoC recovery control added to FAESS.

that the energy variation is proportional to  $D_{fa}$ . The SoC variation also matches the analytical estimation by (22), namely  $(D_{fa}/k_{i,sq} \cdot \Delta P_L)/E_{nom} = (2/10 \cdot 0.5)/6.8 = 1.47\%$ , which is also close to the curves in Fig. 13.

#### D. Case 4: With SoC Recovery Control for FAESS

In addition to the inertia and damping term ( $H_{fa} = 5$  s,  $D_{fa} = 10$  p.u.), a SoC recovery control loop is added to FAESS. As shown in Fig. 34, for the same load change, the frequency nadir is 59.2 Hz at  $t = 37.9$  s, which is close to the results in Fig. 31. However, the power of FAESS gradually decreases to zero and its SoC returns to 0.5, while the emulated gradually picks up all the power mismatch in steady state. For the selected PI parameters in the SoC recovery control, the impact on power and frequency waveform is almost negligible, while improper PI design may worsen the frequency performance or even result in second frequency dip as the conventional event-based virtual inertia control [5].

## VII. CONCLUSION

This article introduced a general framework of control and design of VSM in low-inertia power system, considering the limitation of energy storage in response speed and energy capacity. Based on the theoretical analysis and test results, we draw the following conclusions.

- 1) The inertia-damping and governor control of a synchronous generator emulated by FAESS and SAESS, respectively, well match the operating limitation and characteristics of energy storage in energy capacity and response speed.
- 2) The dynamic and steady-state energy variation of FAESS and SAESS for different inertia and damping values is

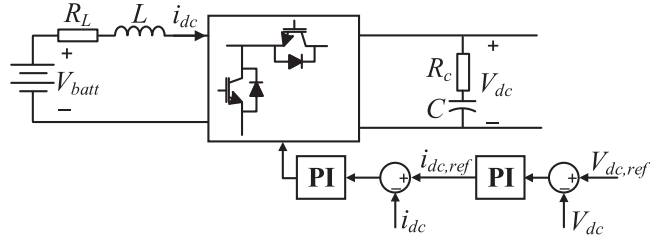


Fig. 35. Diagram of bidirectional dc-dc converter interfacing ESS.

TABLE IV  
PARAMETERS OF DC-DC CONVERTERS IN DC-COUPLED SCHEME USED FOR OFFLINE SIMULATION

Parameters	Values
DC bus voltage $V_{dc}$	1000 V
Nominal storage voltage $V_{batt}$	600 V
FAESS inductance $L$	0.4 mH
FAESS parasitic resistance $R_L$	3 mΩ
FAESS capacitance $C$ for FAESS	4000 μF
FAESS parasitic resistance $R_C$	1 mΩ
FAESS voltage control proportional gain	0.5813
FAESS voltage control integral gain	5.33
FAESS current control proportional gain	0.0007
FAESS current control integral gain	0.5
SAESS inductance $L$	0.4 mH
SAESS parasitic resistance $R_L$	1 mΩ
SAESS current control proportional gain	0.0007
SAESS current control integral gain	0.5

quantified, which provides a guideline for energy storage sizing and control parameter setting in VSM design.

- 3) The energy recovery control designed based on bandwidth separation and stability requirement can restore the energy of FAESS, without undermining frequency control. As a smaller energy storage can synthesize large virtual inertia and damping value, this will significantly reduce the cost and broaden the application of VSM.

## APPENDIX

### A. Parameters of dc-dc converters

In the dc-coupled scheme, bidirectional dc-dc converters are used to interface ESS, as sketched in Fig. 35. Cascaded PI control is utilized by FAESS to maintain the common dc bus voltage as constant, while a single current PI control is adopted by SAESS to achieve constant power. For offline simulation in Section V, the parameters are listed in Table IV.

### B. Parameters of dc-dc converters

In the dc-coupled scheme, one common two-level dc-ac converter with  $LC$  filter is used to realize VSM control. Cascaded PI control in  $dq0$  synchronous reference frame is applied to the converter. For the offline simulation in Section V, the parameters of the converter are listed in Table V.

For the ac-coupled scheme, a two-level dc-ac converter using  $L$  filter is adopted by SAESS, and others with  $LC$  filter are used for FAESS and emulated SG. The parameters in offline simulation and hardware test are listed in Tables V–VII. In the hardware test, a zero-sequence control is also adopted to

TABLE V  
PARAMETERS OF DC-AC CONVERTERS IN DC-COUPLED SCHEME USED FOR OFFLINE SIMULATION

Parameters	Values
Filter inductance $L$	0.6 mH
Inductor parasitic resistance $R_L$	0.6 mΩ
Filter capacitance C	800 uF
Capacitor parasitic resistance $R_C$	2 mΩ
Voltage control proportional gain	0.11
Voltage control integral gain	500
Current control proportional gain	1
Current control integral gain	1

TABLE VI  
PARAMETERS OF DC-AC CONVERTERS IN AC-COUPLED SCHEME USED FOR OFFLINE SIMULATION

Parameters	Values
FAESS inductance $L$	0.6 mH
FAESS parasitic resistance $R_L$	0.6 mΩ
FAESS capacitance C for FAESS	800 uF
FAESS parasitic resistance $R_C$	2 mΩ
FAESS voltage control proportional gain	0.11
FAESS voltage control integral gain	500
FAESS current control proportional gain	0.1
FAESS current control integral gain	0.1
SAESS inductance $L$	1 mH
SAESS parasitic resistance $R_L$	0.6 mΩ
SAESS current control proportional gain	0.0005
SAESS current control integral gain	0.01
SAESS current control proportional gain	1
SAESS current control proportional gain	0.6
SAESS PLL proportional gain	180
SAESS PLL integral gain	1800

TABLE VII  
PARAMETERS OF DC-AC CONVERTERS IN AC-COUPLED SCHEME USED FOR REAL-TIME SIMULATION AND RCP TEST

Parameters	Values
FAESS voltage control proportional gain	0.75
FAESS voltage control integral gain	0.25
FAESS current control proportional gain	2
FAESS current control integral gain	80
SAESS current control proportional gain	5
SAESS current control integral gain	100
SAESS PLL proportional gain	180
SAESS PLL integral gain	1800
SG voltage control proportional gain	1.5
SG voltage control integral gain	0.5
SG current control proportional gain	1.5
SG current control integral gain	60

cancel the circulating current between the paralleled converters connected to a common dc bus.

## REFERENCES

- [1] F. M. Uriarte, C. Smith, S. van Broekhoven, and R. E. Hebner, "Microgrid ramp rates and the inertial stability margin," *IEEE Trans. Power Syst.*, vol. 30, no. 6, pp. 3209–3216, Nov. 2015.
- [2] W. Yang, P. Norrlund, L. Saarinen, J. Yang, W. Zeng, and U. Lundin, "Wear reduction for hydropower turbines considering frequency quality of power systems: A study on controller filters," *IEEE Trans. Power Syst.*, vol. 32, no. 2, pp. 1191–1201, Mar. 2017.
- [3] U. Tamrakar, D. Shrestha, M. Maharjan, B. Bhattacharai, T. Hansen, and R. Tonkoski, "Virtual inertia: Current trends and future directions," *Appl. Sci.*, vol. 7, 2017, Art. no. 654.
- [4] A. Arana "Fast frequency response concepts and bulk power system reliability needs," *NERC Inverter-Based Resource Performance Task Force (IRPTF)*, Mar. 2020. [Online]. Available: <https://www.nrel.gov/grid/ieee-standard-1547/bulk-power-reliability-needs.html>
- [5] L. Meng *et al.*, "Fast frequency response from energy storage systems—A review of grid standards, projects and technical issues," *IEEE Trans. Smart Grid*, vol. 11, no. 2, pp. 1566–1581, Mar. 2020.
- [6] R. Eriksson, N. Modig, and K. Elkington, "Synthetic inertia versus fast frequency response: A definition," *IET Renewable Power Gener.*, vol. 12, no. 5, pp. 507–514, 2018.
- [7] A. Junyent-Ferr, Y. Pipelzadeh, and T. C. Green, "Blending HVDC-link energy storage and offshore wind turbine inertia for fast frequency response," *IEEE Trans. Sustain. Energy*, vol. 6, no. 3, pp. 1059–1066, Jul. 2015.
- [8] O. D. Adeuyi, M. Cheah-Mane, J. Liang, and N. Jenkins, "Fast frequency response from offshore multiterminal VSC-HVDC schemes," *IEEE Trans. Power Del.*, vol. 32, no. 6, pp. 2442–2452, Dec. 2017.
- [9] S. Wang and K. Tomsovic, "Fast frequency support from wind turbine generators with auxiliary dynamic demand control," *IEEE Trans. Power Syst.*, vol. 34, no. 5, pp. 3340–3348, Sep. 2019.
- [10] Q. Hong *et al.*, "Fast frequency response for effective frequency control in power systems with low inertia," *J. Eng.*, vol. 2019, no. 16, pp. 1696–1702, 2019.
- [11] X. Zhao, Y. Xue, and X. Zhang, "Fast frequency support from wind turbine systems by arresting frequency nadir close to settling frequency," *IEEE Open Access J. Power Energy*, vol. 7, pp. 191–202, May 2020.
- [12] W. Liu, G. Geng, Q. Jiang, H. Fan, and J. Yu, "Model-free fast frequency control support with energy storage system," *IEEE Trans. Power Syst.*, vol. 35, no. 4, pp. 3078–3086, Jul. 2020.
- [13] R. K. Varma and M. Akbari, "Simultaneous fast frequency control and power oscillation damping by utilizing PV solar system as PV-STATCOM," *IEEE Trans. Sustain. Energy*, vol. 11, no. 1, pp. 415–425, Jan. 2020.
- [14] D. Duckwitz and B. Fischer, "Modeling and design of df/dt based inertia control for power converters," *IEEE J. Emerg. Sel. Topics Power Electron.*, vol. 5, no. 4, pp. 1553–1564, Dec. 2017.
- [15] J. Driesen and K. Visscher, "Virtual synchronous generators," in *Proc. IEEE Power Energy Soc. Gen. Meeting - Convers. Del. Elect. Energy 21st Century*, Pittsburgh, PA, USA, 2008, pp. 1–3.
- [16] S. D'Arco and J. A. Suul, "Virtual synchronous machines — Classification of implementations and analysis of equivalence to droop controllers for microgrids," in *Proc. IEEE Grenoble Conf.*, Grenoble, France, 2013, pp. 1–7.
- [17] NGESO. "Expert group - grid supporting fast fault current and associated control including virtual synchronous machine approaches," [Online]. Available: <https://www.nationalgrideso.com/codes/grid-code/meetings/vsm-expert-group-meeting>
- [18] State Grid Corporation of China, "State grid corporation of enterprise standards: guidelines for virtual synchronous generator technology," in *Q/GDW 11824-2018*, pp. 1–15, Jul. 2019. [Online]. Available: <http://jsbz.sgcc.com.cn/HTXT/CmsfrontHqSystemAction.do?cmd=detail&id=3099212100000153952>
- [19] Q. Zhong and Y. Zeng, "Universal droop control of inverters with different types of output impedance," *IEEE Access*, vol. 4, pp. 702–712, 2016.
- [20] H. Wu *et al.*, "Small-signal modeling and parameters design for virtual synchronous generators," *IEEE Trans. Ind. Electron.*, vol. 63, no. 7, pp. 4292–4303, Jul. 2016.
- [21] C. Sun, G. Joos, and F. Bouffard, "Identification of low-frequency oscillation mode and improved damping design for virtual synchronous machines in microgrid," *IET Gener. Transmiss. Distrib.*, vol. 13, no. 14, pp. 2993–3001, 2019.
- [22] H. Cheng, Z. Shuai, C. Shen, X. Liu, Z. Li, and Z. J. Shen, "Transient angle stability of paralleled synchronous and virtual synchronous generators in islanded microgrids," *IEEE Trans. Power Electron.*, vol. 35, no. 8, pp. 8751–8765, Aug. 2020.
- [23] Y. Hirase, K. Sugimoto, K. Sakimoto, and T. Ise, "Analysis of resonance in microgrids and effects of system frequency stabilization using a virtual synchronous generator," *IEEE J. Emerg. Sel. Topics Power Electron.*, vol. 4, no. 4, pp. 1287–1298, Dec. 2016.
- [24] L. Huang, H. Xin, and Z. Wang, "Damping low-frequency oscillations through VSC-HVdc stations operated as virtual synchronous machines," *IEEE Trans. Power Electron.*, vol. 34, no. 6, pp. 5803–5818, Jun. 2019.

- [25] G. Li *et al.*, "Analysis and mitigation of subsynchronous resonance in series-compensated grid-connected system controlled by a virtual synchronous generator," *IEEE Trans. Power Electron.*, vol. 35, no. 10, pp. 11096–11107, Oct. 2020.
- [26] J. Liu, Y. Miura, H. Bevrani, and T. Ise, "Enhanced virtual synchronous generator control for parallel inverters in microgrids," *IEEE Trans. Smart Grid*, vol. 8, no. 5, pp. 2268–2277, Sep. 2017.
- [27] T. Wen, D. Zhu, X. Zou, B. Jiang, L. Peng, and Y. Kang, "Power coupling mechanism analysis and improved decoupling control for virtual synchronous generator," *IEEE Trans. Power Electron.*, vol. 36, no. 3, pp. 3028–3041, Mar. 2021.
- [28] K. Shi, W. Song, P. Xu, Z. Fang, and Y. Ji, "Low-voltage ride-through control strategy for a virtual synchronous generator based on smooth switching," *IEEE Access*, vol. 6, pp. 2703–2711, 2017.
- [29] A. Kusko and J. DeDad, "Short-term, long-term, energy storage methods for standby electric power systems," in *Proc. 40th IAS Ann. Meeting. Conf. Rec. Ind. Appl. Conf.*, Kowloon, Hong Kong, 2005, pp. 2672–2678.
- [30] D. Chen, Y. Xu, and A. Q. Huang, "Integration of DC microgrids as virtual synchronous machines into the AC grid," *IEEE Trans. Ind. Electron.*, vol. 64, no. 9, pp. 7455–7466, Sep. 2017.
- [31] X. Hou, Y. Sun, X. Zhang, J. Lu, P. Wang, and J. M. Guerrero, "Improvement of frequency regulation in VSG-based AC microgrid via adaptive virtual inertia," *IEEE Trans. Power Electron.*, vol. 35, no. 2, pp. 1589–1602, Feb. 2020.
- [32] N. Soni, S. Doolla, and M. C. Chandorkar, "Inertia design methods for islanded microgrids having static and rotating energy sources," *IEEE Trans. Ind. Appl.*, vol. 52, no. 6, pp. 5165–5174, Nov./Dec. 2016.
- [33] J. Fang, H. Li, Y. Tang, and F. Blaabjerg, "Distributed power system virtual inertia implemented by grid-connected power converters," *IEEE Trans. Power Electron.*, vol. 33, no. 10, pp. 8488–8499, Oct. 2018.
- [34] Q. Peng, J. Fang, Y. Yang, T. Liu, and F. Blaabjerg, "Maximum virtual inertia from DC-link capacitors considering system stability at voltage control timescale," *IEEE J. Emerg. Sel. Topics Circuits Syst.*, vol. 11, no. 1, pp. 79–89, Mar. 2021.
- [35] X. Xiong, C. Wu, B. Hu, D. Pan, and F. Blaabjerg, "Transient damping method for improving the synchronization stability of virtual synchronous generators," *IEEE Trans. Power Electron.*, vol. 36, no. 7, pp. 7820–7831, Jul. 2021.
- [36] C. Yuan, D. Yang, J. Feng, and C. Liu, "Constrained operation zone of a VSG considering the DC-side power margin," *J. Eng.*, vol. 2019, no. 16, pp. 2563–2568, 2019.
- [37] X. Luo, J. Wang, M. Dooner, and J. Clarke, "Overview of current development in electrical energy storage technologies and the application potential in power system operation," *Appl. Energy*, vol. 137, pp. 511–536, 2015.
- [38] R. Hemmati and H. Saboori, "Emergence of hybrid energy storage systems in renewable energy and transport applications—A review," *Renewable Sustain. Energy Rev.*, vol. 65, pp. 11–23, 2016.
- [39] S. Hajiaghasi, A. Salemmia, and M. Hamzeh, "Hybrid energy storage system for microgrids applications: A review," *J. Energy Storage*, vol. 21, pp. 543–570, 2019.
- [40] J. Fang, Y. Tang, H. Li, and X. Li, "A battery/ultracapacitor hybrid energy storage system for implementing the power management of virtual synchronous generators," *IEEE Trans. Power Electron.*, vol. 33, no. 4, pp. 2820–2824, Apr. 2018.
- [41] R. K. Sarojini, K. Palanisamy, P. Sanjeevikumar, and J. B.-H. Nielsen, "Inertia emulation control technique based frequency control of grid-connected single-phase rooftop photovoltaic system with battery and supercapacitor," *IET Renewable Power Gener.*, vol. 14, no. 7, pp. 1156–1163, 2020.
- [42] Y. Ma, W. Cao, L. Yang, F. Wang, and L. M. Tolbert, "Virtual synchronous generator control of full converter wind turbines with short-term energy storage," *IEEE Trans. Ind. Electron.*, vol. 64, no. 11, pp. 8821–8831, Nov. 2017.
- [43] J. W. Shim, G. Verbić, N. Zhang, and K. Hur, "Harmonious integration of faster-acting energy storage systems into frequency control reserves in power grid with high renewable generation," *IEEE Trans. Power Syst.*, vol. 33, no. 6, pp. 6193–6205, Nov. 2018.
- [44] M. Shi, H. Chen, C. Zhang, F. Mei, J. Fang, and H. Miao, "A virtual synchronous generator system control method with battery SOC feedback," in *Proc. 2nd IEEE Conf. Energy Internet Energy Syst. Integr.*, Beijing, China, 2018, pp. 1–4.
- [45] C. Sun, S. Q. Ali, G. Joos, and F. Bouffard, "Virtual synchronous machine control for low-inertia power system considering energy storage limitation," in *Proc. IEEE Energy Convers. Congr. Expo.*, Baltimore, MD, USA, 2019, pp. 6021–6028.
- [46] B. Wen, D. Boroyevich, R. Burgos, P. Mattavelli, and Z. Shen, "Analysis of D-Q small-signal impedance of grid-tied inverters," *IEEE Trans. Power Electron.*, vol. 31, no. 1, pp. 675–687, Jan. 2016.
- [47] T. Xu, W. Jang, and T. J. Overbye, "Investigation of inertia's locational impacts on primary frequency response using large-scale synthetic network models," in *Proc. IEEE Power Energy Conf. Illinois*, Champaign, IL, USA, 2017, pp. 1–7.
- [48] OSN-32115170-LTO26Ah, "Lithium titanate battery 2.4V 26Ah LTO for communication base station power supply." *OSN Power Energy Limited, China*, [Online]. Available: [osnpower.com/lithium-titanate-battery-2-4v-26ah-lto-for-communication-base-station-power-supply\\_p101.html](http://osnpower.com/lithium-titanate-battery-2-4v-26ah-lto-for-communication-base-station-power-supply_p101.html)
- [49] BMOD0006 E160 B02, "160 V 6F Ultracapacitor Module Datasheet." *Maxwell Technologies, Inc.*, [Online]. Available: [https://www.maxwell.com/images/documents/160vmodule\\_ds\\_3000246-5.pdf](https://www.maxwell.com/images/documents/160vmodule_ds_3000246-5.pdf)
- [50] L. Fan, *Control and Dynamics in Power Systems and Microgrids*, 1st ed. Boca Raton, FL, USA: CRC Press, 2017.
- [51] C. Sun *et al.*, "Design and real-time implementation of a centralized microgrid control system with rule-based dispatch and seamless transition function," *IEEE Trans. Ind. Appl.*, vol. 56, no. 3, pp. 3168–3177, May/Jun. 2020.



**Chu Sun** (Member, IEEE) received the B.Sc. and M.Sc. degrees from Beihang University, Beijing, China, in 2012 and 2015, respectively, and the Ph.D. degree (*on the topic of virtual synchronous machine and microgrid control*) from McGill University, Montreal, QC, Canada, in 2021, all in electrical engineering.

He is currently an Assistant Professor with the School of Automation Science and Electrical Engineering, Beihang University, Beijing, China. He was a Research Assistant with McGill University program and an intern researcher with OPAL-RT Technologies funded by MITACS, working on design, real-time simulation, and implementation of industrial microgrid controller. His research interests include power-electronic converter control and stability analysis for renewable generation, microgrid control, DER integration, motor design, and drives for electrical transportation.



**Syed Qaseem Ali** (Member, IEEE) received the B.Eng. degree from the NED University of Technology, Karachi, Pakistan, in 2007, the M.S. degree in electrical engineering power and control from the Illinois Institute of Technology, Chicago, IL, USA, in 2010, and the Ph.D. degree in electrical engineering (*in the control and design of integrated battery chargers for electric vehicles*) from McGill University, Montreal, QC, Canada, in 2018.

He was with OPAL-RT Technologies as a Lead Simulation Expert for the Distribution and Generation team in the Application eXpertise and Electrical Simulation division and is currently employed as a Power System Consultant with OSI Digital Grid Solutions. Before joining OPAL-RT, he worked as a Graduate Research Assistant with McGill University, Research Engineer with King Saud University, Riyadh. His current research interests include microgrid controls, DER integration, DERMS, EV charger design and control, and power electronic converters for renewable energy applications.



**Geza Joos** (Life Fellow, IEEE) received the Graduate degree in electrical engineering from Concordia University in 1972, and the M.Eng. and Ph.D. degrees in electrical engineering from McGill University, Montreal, QC, Canada in 1974 and 1987 respectively.

He has been a Professor with the Department of Electrical and Computer Engineering, McGill University, since 2001. He has been the NSERC/Hydro-Quebec Industrial Research Chair on the Integration of Renewable Energies and Distributed Generation into the Electric Distribution Grid, since 2009, and a

Canada Research Chair in Powering Information Technologies, since 2004. He was previously with ABB, the Université du Québec, and Concordia University (Montreal, Canada). He has a consulting experience in the areas of power electronic converters, with applications to power systems. His research interests include distributed energy resources, including renewable energy resources, advanced distribution systems, and microgrids.

Prof. Joos is a Secretary of CIGRE Study Committee C6 on Distributed Energy Resources and Active Distribution Systems, and active in IEEE Power and Energy Society working groups on power electronic applications to power systems and IEEE Standards Association working groups on distributed energy resources and microgrids. He is a Fellow of CIGRE, the Canadian Academy of Engineering, and the Engineering Institute of Canada.



**François Bouffard** (Senior Member, IEEE) received the B.Eng.(Hons.) and Ph.D. degrees in electrical engineering from McGill University, Montreal, QC, Canada, in 2000 and 2006, respectively.

In 2006, he took up a lectureship with the School of Electrical and Electronic Engineering, The University of Manchester, Manchester, U.K. In 2010, he was with McGill University as an Assistant Professor. His research interests include power system modeling, economics, reliability, control, and optimization.

Dr. Bouffard is a Licensed Engineer in the province of Quebec, Canada, and a member of the IEEE Power and Energy Society.